

1 **Benchmark study using a multi-scale, multi-methodological approach for the**
2 **petrophysical characterization of reservoir sandstones**

3
4 Peleg Haruzi^{1,2}, Regina Katsman¹, Matthias Halisch³, Nicolas Waldmann¹, and Baruch Spiro^{1,4}

5
6 ¹The Dr. Moses Strauss Department of Marine Geosciences, Faculty of Natural Sciences, The University of
7 Haifa, Haifa, Mount Carmel 3498838, Israel

8 ²Agrosphere Institute, IBG-3, Institute of Bio- and Geosciences, Forschungszentrum Jülich GmbH, Germany

9 ³Leibniz Institute for Applied Geophysics, Dept. 5 – Petrophysics & Borehole Geophysics, Stilleweg 2, D-
10 30655 Hannover, Germany

11 ⁴Department of Earth Sciences, Natural History Museum, Cromwell Road, London SW7 5BD, UK

12
13
14 *Correspondence to:* Regina Katsman (rkatsman@univ.haifa.ac.il)

15 Matthias Halisch (Matthias.Halisch@leibniz-liag.de)

16
17
18
19 **Keywords:** multi-methodological approach, permeability, petrography, petrophysics, 3D imaging, pore-scale
20 modelling, upscaling, ~~REV analysis~~, benchmark study.

Deleted: semivariogram modelling,

23
24
25
26
27
28
29
30
31
32
33
34
35
36
37
38
39
40
41
42
43
44
45
46
47
48

Abstract

This paper presents a detailed description and evaluation of a multi-methodological petrophysical approach for the comprehensive multiscale characterization of reservoir sandstones. The suggested methodology enables the identification of links between Darcy-scale permeability and an extensive set of geometrical, textural and topological rock descriptors quantified at the pore scale. This approach is applied to the study of samples from three consecutive sandstone layers of Lower Cretaceous age in northern Israel. These layers differ in features observed at the outcrop, hand specimen, petrographic microscope and micro-CT scales. Specifically, laboratory porosity and permeability measurements of several centimetre-sized samples show low variability in the quartz arenite (top and bottom) layers but high variability in the quartz wacke (middle) layer. The magnitudes of this variability are also confirmed by representative volume sizes and by anisotropy evaluations conducted on micro-CT-imaged 3D pore geometries. Two scales of directional porosity variability are revealed in quartz arenite sandstone of the top layer: the pore size scale of ~0.1 mm in all directions, and ~3.5 mm scale related to the occurrence of high- and low-porosity horizontal bands occluded by Fe oxide cementation. This millimetre-scale variability controls the laboratory-measured macroscopic rock permeability. More heterogeneous pore structures were revealed in the quartz wacke sandstone of the intermediate layer, which shows high inverse correlation between porosity and clay matrix in the vertical direction, attributed to depositional processes and comprises an internal spatial irregularity. Quartz arenite sandstone of the bottom layer is homogenous and isotropic in the investigated domain revealing porosity variability at a ~0.1 mm scale, which is associated with the average pore size. Good agreement between the permeability upscaled from the pore-scale modelling and the estimates based on laboratory measurements is shown for the quartz arenite layers. The proposed multi-methodological approach leads to an accurate petrophysical characterization of reservoir sandstones with broad ranges of textural, topological and mineralogical characteristics and is particularly applicable for describing anisotropy and heterogeneity of sandstones on various rock scales. The results of this study also contribute to the geological interpretation of the studied stratigraphic units.

Deleted: links to

Deleted: semivariogram analyses

Deleted: by applying a semivariogram analysis to

Deleted: 100 μ

Deleted: 1.6

Deleted: scale due

Deleted: in pore size corresponds is found to control

Deleted: (

Deleted: -)

Deleted: along horizontal layers

Deleted:

Deleted: at the different scales: at the pore size scale and at the larger scale of porous “lenses” originated in presence of patchy clay deposition

Deleted: shows stationarity

Deleted: y

Deleted: of pore cross-section

Deleted: at

Deleted: studied

Deleted:

Deleted: of the samples studied

70 1. Introduction

71 Permeability is an effective property of a reservoir rock that varies enormously over a wide range of
72 rock length scales, attributed to a hierarchy of dominant sedimentary depositional features (Norris and Lewis,
73 1991; Nordahl and Ringrose, 2008; Ringrose and Bentley, 2015). Permeability should thus be properly
74 upscaled through the following sequence of scales (Nordahl and Ringrose, 2008; Ringrose and Bentley, 2015
75 and references therein): (1) from the pore scale (the micro scale, typically microns to millimetres) to the
76 representative elementary volume of a single lamina (the macro scale, typically millimetres to centimetres,
77 e.g., Wildenschild and Sheppard, 2013; Andrä et al., 2013b
78 ; Bogdanov et al., 2011; Narsilio et al., 2009); (2) to the scale of geological heterogeneity, e.g., the scale of a
79 stratigraphic [unit](#) (decimetres to decametres, e.g., Jackson et al. 2003; Nordahl et al. 2005); and (3) to the field
80 scale or the scale of an entire reservoir or aquifer (hundreds of metres to kilometres) (Haldorsen and Lake
81 1984; Rustad et al., 2008). Pore scale imaging and modelling enable us to relate macroscopic permeability to
82 basic microscopic rock descriptors (Kalaydjian, 1990; Whitaker, 1986; Cerepi et al., 2002; Haoguang et al.,
83 2014; Nelson, 2009). Therefore, the first stage in the above sequence is crucial for successful upscaling to the
84 [overall](#) reservoir scale permeability.

Deleted: column

85 Over the past few decades, 3D pore scale imaging and flow simulations (Bogdanov et al., 2012; Blunt
86 et al., 2013; Cnudde and Boone, 2013; Wildenschild and Sheppard, 2013; Halisch, 2013a) have started to
87 serve as a reliable method for rock characterization. The advantages of these techniques are their non-
88 destructive character and their capability to provide reliable information about the real pore-space structure
89 and topology of rocks that is impossible to obtain using the conventional experimental methods (e.g., Arns et
90 al., 2007; Knackstedt et al., 2010; Blunt et al., 2013). However, despite its importance, the upscaling from the
91 pore scale is sometimes omitted; as a result, effective petrophysical rock characteristics (e.g., porosity, surface
92 area, and permeability) are often evaluated at the macro scale through only conventional laboratory
93 experiments, which often suffer from errors due to local heterogeneities, anisotropy, or an insufficient number
94 of samples (e.g., Meyer, 2002; Halisch, 2013a).

Deleted: final

95 Digital 3D micro scale core analysis should also become a necessary technique for rocks that are
96 difficult to characterize due to various reasons (e.g., for tight sandstones, Liu et al., 2017; Du et al., 2018;
97 Munawar et al., 2018; Zhang et al., 2019), or for those with inhomogeneous or anisotropic pore space (e.g.,

100 Meyer, 2002; Farrel et al., 2014). Preferential fluid flow pathways are inherently connected to rock
101 microstructure, formed by depositional sedimentary structures such as pore shapes and their preferential
102 orientation (Sato et al., 2019) or lamination (Lewis et al., 1988). Those can be modified with time by
103 dissolution of grains, by grain rearrangement and pore collapse (Halisch et al., 2009; Clavaud et al., 2008), by
104 cementation (Louis et al., 2005), or by deformation structures (fractures). The later may drastically alter the
105 host rock depositional porosity pattern and create new permeability pathways (Zhu et al., 2002; Farrel et al.,
106 2014).

Deleted: Pore-scale modelling is mainly necessitate when capillary forces dominate flow processes (Ringrose and Bentley, 2015)....

107 The present paper provides a detailed description and evaluation of a multi-methodological
108 petrophysical approach for the comprehensive multiscale characterization of reservoir sandstones. The
109 proposed approach includes petrography, gas porosimetry and permeametry, mercury intrusion porosimetry,
110 3D imaging and image analysis, and flow modelling at the pore-scale. The suggested computational workflow
111 enables the identification of Darcy scale permeability links to an extensive set of geometrical, textural and
112 topological rock descriptors, quantified at the pore scale by deterministic methods. The approach presented
113 herein is important for the identification of anisotropy and inhomogeneity. Ultimately, this approach is applied
114 to the study of three different consecutive sandstone layers of Lower Cretaceous age in northern Israel.

Deleted: semivariogram analysis

115 The multi-methodological validation procedure is significant for properly upscaling permeability from
116 the micro scale to the macro scale (Ringrose and Bentley, 2015). This validation, thereby, allows an accurate
117 petrophysical analysis of reservoir sandstones with broad ranges of textural and topological characteristics.
118 The findings contribute also to the current geological knowledge regarding non-marine sandstones of Lower
119 Cretaceous age (e.g., Akinlotan, 2016; 2017; 2018; Li et al., 2016; Ferreira et al., 2016) and specifically
120 regarding the studied stratigraphic unit.

Deleted: at various rock scales

Deleted: The present study uses

Deleted: by applying it

Deleted: in

Deleted: detailed

Deleted: The approach presented herein is especially important for the detection of anisotropy and the identification of its origin at various rock scales.

122 2. Geological setting

123 The study is based on samples collected from a steep outcrop at Wadi E'Shatr near Ein Kinya on the
124 southern slopes of Mt. Hermon (Figure 1). The outcrop consists of sandstones from the Lower Cretaceous
125 Hatira Formation (Sneh and Weinberger, 2003). This formation (Fm.) acts as a reservoir rock for hydrocarbons
126 in Israel (Figure 1a), both onshore, namely, Heletz (Grader and Reiss, 1958; Grader, 1959; Shenhav, 1971,

139 Calvo, 1992; Calvo et al., 2011), and offshore, namely, Yam Yafo (Gardosh and Tannenbaum, 2014; Cohen,
140 1971; Cohen, 1983).

141 The Hatira Fm. is the lower part of the Kurnub Group (Figure 1d) of Lower Cretaceous (Neocomian –
142 Barremian) age. The Hatira Fm. nomenclature used in Israel and Jordan is equivalent to Grès de Base in
143 Lebanon (Massaad, 1976). This formation occurs in Israel in outcrops from the Eilat area along the rift valley,
144 in the central Negev, and in the northernmost outcrops on Mount Hermon; it forms part of a large Palaeozoic
145 – Mesozoic platform and continental margin deposits in north-eastern Africa and Arabia. The Hatira Fm.
146 consists of siliciclastic units, typically dominated by quartz-rich sandstones (Kolodner et al., 2009 and
147 references therein). The underlying Palaeozoic sandstones cover large areas in North Africa and Arabia from
148 Morocco to Oman; these sandstones overlie a Precambrian basement affected by Neoproterozoic (pan African)
149 orogenesis (Garfunkel, 1988, 1999; Avigad et al., 2003, 2005). The lower Palaeozoic sandstones in Israel and
150 Jordan originated from the erosion of that Neoproterozoic basement, the Arabian-Nubian Shield, with
151 contributions from older sources. These lower Palaeozoic sandstones (Cambrian and Ordovician) are
152 described as first-cycle sediments (Weissbrod and Nachmias, 1986; Amireh, 1997; Avigad et al., 2005).
153 Exposures of the Hatira Fm. in the Central Negev, the Arava Valley, Eilat and Sinai were originally defined
154 as the Wadi (Kurnub) Hatira Sandstone (Shaw, 1947). The largely siliciclastic section of the Hatira Fm. is
155 intercalated with carbonates and shales representing marine incursions that increase towards the north
156 (Weissbrod, 2002).

157 The Lower Cretaceous sandstones of the Kurnub Group are described as super mature, cross-bedded,
158 medium- to fine-grained, moderately sorted to well-sorted quartz arenites with a high zircon-tourmaline-rutil
159 (ZTR) index (for more details, see Kolodner, 2009). Earlier observations indicated the relatively scarce
160 occurrence of siltstones and claystones compared to sandstones (Massaad, 1976; Abed, 1982; Amireh, 1997).
161 These Lower Cretaceous sandstones are mainly the recycled products of older siliciclastic rocks throughout
162 the Phanerozoic; the sand was first eroded from the surface of the pan African orogeny ca. 400 Ma prior to its
163 deposition in the Lower Cretaceous sediments (Kolodner et al., 2009).

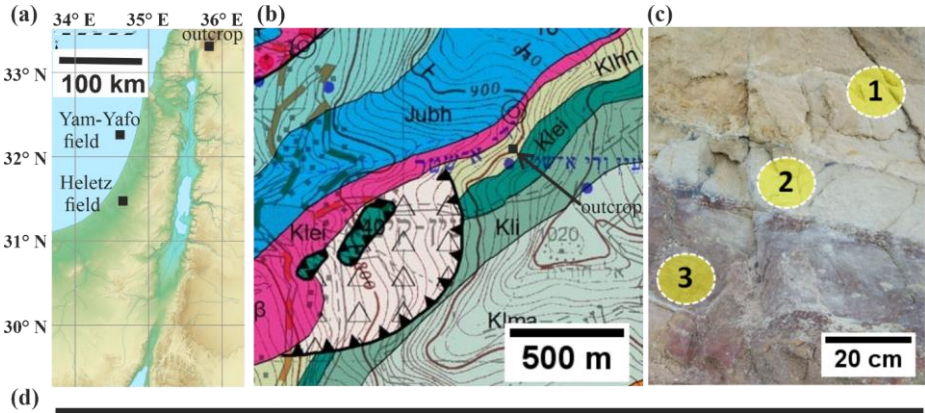
164 The Mount Hermon block was located at the southern border of the Tethys Ocean during the Early
165 Cretaceous (Bachman and Hirsch, 2006). A paleo-geographical reconstruction indicates that the sandy Hatira
166 Fm. (Figure 1) was deposited in a large basin, which included both terrestrial and coastal environments such

Deleted: ;

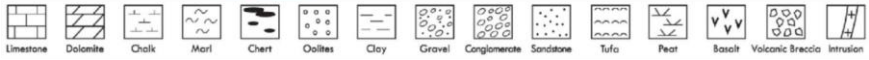
168 as swamps and lagoons (Sneh and Weinberger, 2003). The Hermon block, located next to the Dead Sea
169 Transform, was rapidly uplifted during the Neogene (Shimron, 1998). The area is marked by intense erosion,
170 which resulted in extensive outcrops such as those near Ein Kinya on the south-eastern side of Wadi E'Shatr
171 (Figure 1).

172 The Kurnub Group in the study area (Figure 1b, d) consists of a volcanic sequence at its base that is
173 overlain with an angular unconformity by sandstone and clay layers of the Hatira Fm.; the upper unit consists
174 of limestone, marl and chalk – the Nabi Said Fm. (Sneh and Weinberger, 2003). At the section [investigated](#)
175 [by](#) Saltzman (1968), which is approximately 100 m SW of the sampling area of the present study, the 58 m
176 thick variegated sandstone is interbedded with layers of clay and clay-marl. The sandy component is white-
177 yellow-brown/red and consists of largely angular, poorly sorted, fine- to coarse-grained quartz sand.
178 Individual sandstone layers are cemented by Fe oxide (Fe-ox). The outcrops show lenticular benches 0.2 m -
179 1.0 m thick. The clay-rich interlayers are grey and normally silty and brittle. Locally, these layers contain
180 lignite. The outcrop investigated and the specific beds sampled in the present study are shown in Figure 1c.

Deleted: of



| SERIES - STAGE | | SYMBOL | THICK. m | LITHOLOGY | LITHOSTRATIGRAPHY | |
|------------------|---------------------|------------|-------------|-----------|--|--------|
| | | | | | MAPPING UNITS | GROUP |
| LOWER CRETACEOUS | APTIAN | Kli | 45 | | Hidra Formation | JUDEA |
| | | Klei | | | Ein El Assad Formation | |
| | NEOCOMIAN-BARREMIAN | Kln + Klih | 85 | | Hatira & Nabi Sa'id formations | KURNUB |
| | | Kliβ | | | Volcanic sequence: basaltic flows, pyroclastics & lacustrine sediments | |
| JURASSIC | OXFORDIAN | Jubh | 225 | | Be'er Sheva & Haluza formations | ARAD |
| | | Juk | 110 | | Kidod Formation | |
| | | | | | | |



182

183 **Figure 1:** Geographical and geological settings. (a) Schematic relief map of Israel (modified from www.mapsland.com).

184 (b) Geological map of Ein Kinya. The Hatira Fm. sandstone and the overlying limestone and marl of the Nabi Said Fm.

185 are marked as Kln (map is adopted from Sneh and Weinberger, 2014). (c) Outcrop of the Lower Cretaceous Hatira Fm.
186 sandstones (Kln) at Ein Kinya. The studied sandstone layers have distinct colours: yellow-brown (1), grey-green (2),
187 and red-purple (3). (d) Stratigraphic table of the geological map (modified from Sneh and Weinberger, 2014).

188 **3. Methods**

189 **3.1. Sample description**

190 Samples were extracted from three consecutive layers of different colours from a stratigraphic sequence
191 (Figures 1c, 1d). The lower layer (3) is ~1.5 m thick and consists of sandstone that is light (pale) red-purple in
192 colour with undulating bedding planes between the sub-layers. The middle layer (2) is composed of grey –
193 green shaly sandstone that is 20 cm thick with dark horizons at the bottom and top. The upper layer (1)
194 comprises 1.5 m thick homogenous brown-yellow sandstone. Large sample blocks of ~10–20 cm size were
195 collected from these three layers, and the directions perpendicular to the bedding planes (defined as the z-
196 directions in our study) were noted. Subsequently, in the laboratory, smaller sub-samples (described below)
197 were prepared from these large samples for textural observations and various analytical measurements and
198 computations. In total, 7 sub-samples from the top layer, 8 sub-samples from the middle layer and 4 sub-
199 samples from the bottom layer were investigated in the laboratory (Table 2).

200 **3.2. Laboratory and computational methods for rock characterization**

201 The integrated analytical programme designed for this study includes the following laboratory
202 measurements and computations conducted at different scales (from the micro scale reflecting the scale of
203 individual pores and grains to the core scale reflecting the scale of the laminas at the outcrop) (Table 1).
204 Specimens ~5–7 cm in size were investigated by petrographic and petrophysical lab methods. Sub-samples ~1
205 cm in size were retrieved from the aforementioned plugs for investigation by 3D imaging, digital image
206 analysis and simulation techniques (described in detail below).

207 Petrographic and petrophysical analysis (#1–7 in Table 1) were conducted following the RP40 guidelines
208 (Recommended Practices for Core Analysis, API, 1998), giving detailed information on theory, advantages
209 and drawbacks of each method. An extended computational workflow (#8 in Table 1) combines several
210 methods that may contain some variability in their application for the rock characterization. Those are
211 described in more detail below.

Deleted: .

Deleted: ÷

Deleted: more

Deleted: have been

Deleted: E

217 **Table 1.** Laboratory methods employed and petrophysical characteristics determined from these methods

| Method | Determined petrophysical characteristics |
|---|--|
| 1. Scanning electron microscopy (SEM) | Mineral abundance, grain surface characterization of matrix and cementation |
| 2. Grain size analysis (Laser diffraction) | Grain size distribution (<i>GSD</i>) |
| 3. X-ray diffraction (XRD) | Mineral components |
| 4. Nitrogen gas porosimetry | Porosity (ϕ) |
| 5. Steady state permeametry | Permeability (1D) (κ) |
| 6. Mercury intrusion porosimetry (MIP) | Pore throat size distribution (<i>PTSD</i>), specific surface area (<i>SSA</i>), characteristic length (l_c), pore throat length of maximal conductance (l_{max}), permeability (κ) |
| 7. Optical microscopy Plane-parallelized (PPL) and cross-parallelized (XPL) and reflected-light (RL) microscopy, binocular (BINO). | Mineral abundance, grain surface characterization, cementation |
| 8. Extended computational workflow: Digital image analysis (DIA) | Porosity (ϕ), pore specific surface area (<i>PSA</i>), tortuosity (τ), pore size distribution (<i>PSD</i>), connectivity index (<i>CI</i>), micro-CT predicted porosity from MIP |
| Fluid flow modelling | Permeability tensor ($\vec{\kappa}$), tortuosity (τ) |

Deleted: Semivariogram analyses¶

Deleted: Range of spatial correlation of pore structures ¶

218

219 Petrographic descriptions of rock compositions and textures at the micro scale, notably those of the fine
220 fraction, were performed using scanning electron microscopy (*JCM-6000 Bench Top SEM device*; e.g.,
221 Krinsley et al., 2005) using both backscatter and secondary electron modes.

222 Thin-section optical microscopy (*Olympus BX53 device*, e.g., MacKenzie et al., 2017) was used to
223 estimate the mineral abundance and surface features of the grains, and the mineralogical and textural features
224 of matrix and cement. Grain size distributions were determined by a laser diffraction particle size analyser (*LS*

227 13 320; e.g., Wang et al., 2013). X-ray diffraction (*Miniflex 600 device by Rigaku*; e.g., Asakawa et al., 2020)
228 was applied to powdered samples to determine their mineralogical composition.

229 Effective porosity and permeability were evaluated on dried cylindrical samples (2.5 cm in diameter and
230 5-7 cm in length). Effective porosity (ϕ) was measured using a steady-state nitrogen gas porosimeter produced
231 by Vinci Technologies (*HEP-E, Vinci Technologies*; e.g., Viswanathan et al., 2018). Absolute permeability (κ)
232 was measured by using a steady-state nitrogen gas permeameter (*GPE, Vinci Technologies*; e.g., Tidwell et
233 al., 1999).

234 Mercury intrusion porosimetry (*Micromeritics AutoPore IV 9505*, which considers pore throats larger
235 than 0.006 μm ; e.g., Giesche, 2006) was applied to dried cylindrical samples $\sim 1 \text{ cm}^3$ in size to evaluate the
236 following parameters (Table 1):

- 237 • Pore throat size distribution (*PTSD*, Lenormand, 2003).
- 238 • Specific surface area (*SSA*): the pore surface to bulk sample volume (Rootare and Prenzlöw, 1967;
239 Giesche, 2006).
- 240 • Characteristic length (l_c): the largest pore throat width (obtained from the increasing intrusion
241 pressure) at which mercury forms a connected cluster (Katz and Thompson, 1987).
- 242 • Pore throat length of maximal conductance (l_{max}): defines a threshold for the pore throat size l at
243 which all connected paths composed of $l \geq l_{max}$ contribute significantly to the hydraulic
244 conductance, whereas those with $l < l_{max}$ may completely be ignored (Katz and Thompson,
245 1987).
- 246 • Permeability (Katz and Thompson, 1987):

$$247 \quad \kappa = \frac{1}{89} l_{max}^2 \frac{l_{max}}{l_c} \phi S(l_{max}) \quad (1)$$

248 where $S(l_{max})$ is the fraction of connected pore space that is composed of pore throat widths of size l_{max} and
249 larger. This [model](#) (Katz and Thompson, 1987), which was derived from percolation theory (Ambegaokar et
250 al., 1971), is applicable for sandstones with a broad distribution of local conductances with short-range
251 correlations only.

252 An extended computational workflow (similar to the procedure presented by Boek and Venturoli, 2010;
253 Andrä et al., 2013a,b) (Figure 2) serves as one of the main methodologies in our study to upscale permeability

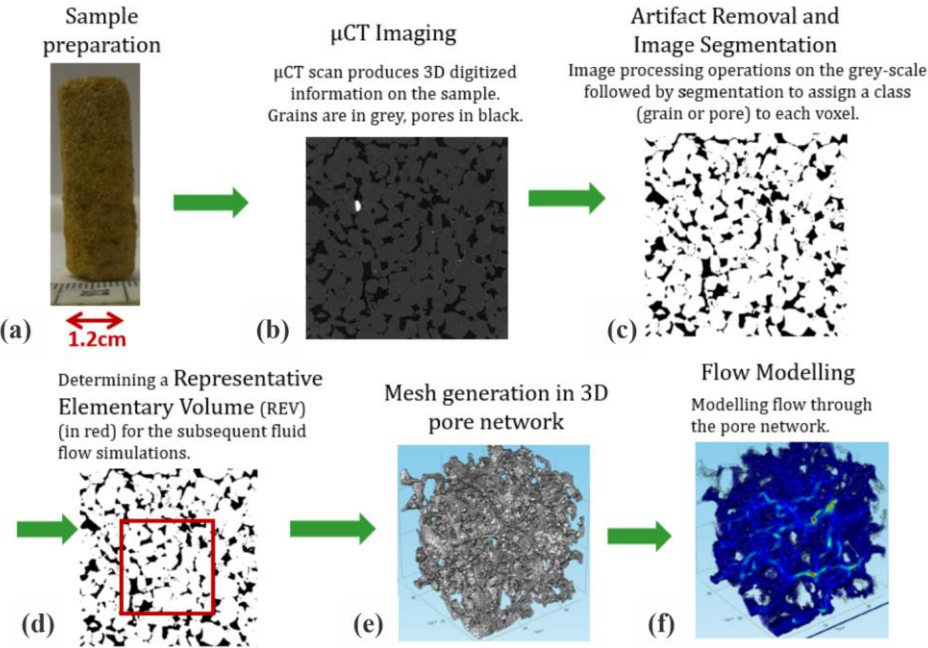
Deleted: approach

255 [and derive microscopic rock descriptors](#). It includes 3D micro-CT imaging of porous samples, digital image
256 processing and segmentation, statistical analyses for the determination of representative elementary volumes,
257 and pore-scale flow modelling through the 3D pore geometry of the rock. First, cylindrical subsamples 4-8
258 mm in diameter and 5-10 mm in length were retrieved from the larger samples studied in the laboratory ([Figure](#)
259 [2a](#)) and were scanned non-destructively (Figure 2b) by using a *Nanotom 180 S* micro-CT device (*GE Sensing*
260 *& Inspection Technologies, phoenix/X-ray product line*, Brunke et al., 2008). The achieved voxel size of the
261 data sets was 2.5 μm or 5 μm (isotropic), suitable for imaging pore throats that effectively contribute to the
262 flow in the studied type of sandstone (e.g., Nelson, 2009). Afterwards, all data sets were filtered for de-noising,
263 X-ray artefact removal and edge enhancement (Figure 2c). The post-processed images scanned with 2.5 μm
264 resolution had an edge length of 1180 voxels or 2950 μm . Image artefacts were processed as described by
265 Wildenschild and Sheppard (2013). Beam hardening artefacts were removed by applying the best-fit quadratic
266 surface algorithm (Khan et al., 2016) to each reconstructed 2D slice of the image. Ring artefact reduction and
267 image smoothing (with preservation of sharp edge contrasts) were performed using a non-local means filter
268 (Schlüter, 2014). Segmentation was performed to convert the grey-scale images obtained after image filtering
269 into binary images to distinguish between voids and solid phases (Figure 2c). The local segmentation approach,
270 which considers the spatial dependence of the intensity for the determination of a voxel phase, was used in
271 addition to a histogram-based approach (Iassonov et al., 2009; Schlüter et al., 2014). [Segmentation was](#)
272 performed by the converging active contours algorithm (Sheppard et al., 2004), a combination of a watershed
273 (Vincent et al., 1991) with an active contour algorithm (Kass et al., 1988).

274

Deleted: Two-phase s

276
277



278

279 **Figure 2:** Extended computational workflow. See text for more details. Images (e) and (f) are adopted from
280 Bogdanov et al. (2012).

281 Simulations involving the real geometry of an imaged rock are computationally power and time
282 consuming. Therefore, the determination of a representative elementary volume (REV) is required (Figure 2d),
283 assuming that porous media are homogeneous at REV dimensions (Bear, 2013), to perform fluid flow
284 simulations. Porosity, a basic macroscopic structural property of porous media, is used here for the estimation
285 of an REV (Bear, 2013; Halisch, 2013a; Tatomir et al., 2016) based on its correlation with permeability
286 (Kozeny, 1927; Carman, 1937) (see discussion on this issue in the Discussion Sect.).

Deleted: . A REV is required in the current study

288 A “classic” REV approach was used that claims that the REV is attained when porosity fluctuations in
 289 the sub-volumes that grow isotropically in three orthogonal directions become sufficiently small (Bear, 2013;
 290 Halisch, 2013a, b). Practically, a large number of randomly distributed cubes were analysed through the entire
 291 3D sample for their image porosity (IP). The chosen initial cube size (with an edge length of 10 pixels in our
 292 case) was increased by 10-100 voxels. The REV size was specified when agreements between the mean and
 293 median IP values as well as saturation in the IP fluctuations were attained.

294 Further, the representative binary 3D image (REV) of the pore space was spatially discretised by
 295 tetrahedrals with *Materialize software (Belgium)* (Figure 2e). This step is required for importing the REV into
 296 the FEM-based modelling software (*Comsol Multiphysics simulation environment, v5.2a*). Stokes flow ($Re \ll$
 297 1) is simulated (Table 1) in the pore network (Figure 2f) by the following equations (e.g., Narsilio et al., 2009;
 298 Bogdanov et al., 2011):

299 Stokes equation: $-\nabla p + \mu \nabla^2 \bar{u} = 0$ (2)

300 Continuity equation: $\nabla \cdot \bar{u} = 0$ (3)

301 where ∇p is the local pressure gradient, \bar{u} is the local velocity vector in the pore space and μ is the dynamic
 302 fluid viscosity. Fixed pressures ($p=const$) were specified at the inlet and outlet boundaries of the fluid domain
 303 with a constant pressure gradient of 2.424 Pa/mm over the domain, prescribed in all the simulations for
 304 consistency. At the internal pore walls and at the lateral domain boundaries, no-slip boundary conditions ($\bar{u} =$
 305 0) were imposed (e.g., Guibert et al., 2016). These boundary conditions are also used to simulate the flow
 306 setup in a steady-state experimental permeameter (e.g., Renard et al., 2001). The macroscopic fluid velocity
 307 $\langle \bar{v} \rangle$ was evaluated by volumetrically averaging the local microscopic velocity field (e.g., Narsilio, 2009;
 308 Guibert et al., 2016). Then, from the average macroscopic velocity vectors v_i^j in three orthogonal i -directions
 309 corresponding to the pressure gradients ∇p_j imposed in j -directions, the full 3D second rank upscaled
 310 permeability tensor \bar{k} can be found:

311
$$\begin{pmatrix} v_x^x & v_x^y & v_x^z \\ v_y^x & v_y^y & v_y^z \\ v_z^x & v_z^y & v_z^z \end{pmatrix} = -\frac{1}{\mu \phi} \begin{pmatrix} \kappa_{xx} & \kappa_{xy} & \kappa_{xz} \\ \kappa_{yx} & \kappa_{yy} & \kappa_{yz} \\ \kappa_{zx} & \kappa_{zy} & \kappa_{zz} \end{pmatrix} \begin{pmatrix} \nabla p_x & 0 & 0 \\ 0 & \nabla p_y & 0 \\ 0 & 0 & \nabla p_z \end{pmatrix} \quad (4)$$

Deleted: Two approaches were used in this study to estimate the REV (Halisch, 2013a,b). In the

Deleted: ,

Deleted: to determine

Deleted: according flow

Deleted:)

Deleted: (with a 1180 voxel edge length in our case)

Deleted: The results of the REV estimation by this classic approach can be found in Appendix A.

Deleted: A more advanced “directional” REV approach can capture porosity changes in a specific direction caused by microscopic structural features, such as grain packing, cracks, and textural effects (Halisch, 2013b). The IP is calculated slice by slice across the segmented image in each orthogonal direction. ¶ Semivariogram analysis was also conducted to estimate the REV. Semivariogram (Cressie, 1985) defines the relation between a spatially varying property (porosity in our case) and a lag distance (a Cartesian distance between the points in the studied domain). The semivariogram value increases when the values of the studied parameter become more dissimilar. Semivariogram, $\gamma(h)$, is based on the difference in values of the studied property between all combinations of pairs of data points, x_i and y_i , in the studied domain and is defined by: ¶

$$\gamma(h) = \frac{1}{2N(h)} \sum_{i=1}^{N(h)} (x_i - y_i)^2 \quad (2), ¶$$

where $N(h)$ is the number of pairs, and h is the lag distance. A semivariogram describing a single variability structure is characterized by a sill (a plateau) in which γ corresponds to the total variability of the sample, and by the range (of correlation) in h at which γ reaches the sill value (usually ~95 % of the sill value). Due to the spatial continuity of the CT dataset, a lag increment of a voxel size set by the CT acquisition resolution, was chosen for calculation of the semivariogram, thus producing a large amount of data point pairs at each lag to get a significant mean (Ploner, 1999). A non-zero intercept in the semivariogram (nugget effect) may exist due to variability at lengths smaller than the lag distance and due to noisy data. For CT data, natural variations below the fixed resolution limit are invisible for the variography analysis. Therefore, in CT data the nugget effect may be observed only due to measurement error inherent to measuring devices. In a case they are small, the semivariogram will approximately have a zero intercept. ¶ ...

Moved down [1]: z-direction of CT specimen used in this analysis is perpendicular to the natural layering of the sandstone identified in the outcrop and in the petrographic observations. x- and

Deleted: The application of the semivariogram analysis using all data points (the voxels) distributed at multiple 3D sub-volume domains, is computationally intensive as the typical CT dataset ...

Deleted: 7

Deleted: 8

Deleted: also

Deleted: -

Deleted: 9

440 where z-direction of the CT specimen used in this analysis is perpendicular to the natural layering of the
 441 sandstone identified in the outcrop and in the petrographic observations. x- and y- orthogonal directions lie in
 442 the horizontal plane, with an azimuth chosen randomly. The permeability tensor is symmetrized by:

$$443 \quad \bar{\kappa}_{sym} = \frac{1}{2}(\bar{\kappa} + \bar{\kappa}^T) \quad (5)$$

444 Additional permeability tensor simulations in the multiple REV sub-volumes of one of the investigated
 445 samples have been performed by using the FlowDict module (Linden et al., 2015; 2018) of the GeoDict toolbox
 446 (Wiegmann, 2019). Pre-processing as well as boundary conditions are identical to those used in Comsol setup.

447 Tortuosity (τ ; Bear, 2013; Boudreau, 1996) was calculated separately in the x-, y- and z-directions in
 448 the meshed domain using the particle tracing tool of *Comsol Multiphysics software* (an additional method for
 449 deriving τ is presented later in this section).

450 3D image analysis (Table 1) was conducted on a high-quality, fully segmented micro-CT image (edge
 451 length of 2950 μm scanned at a 2.5 μm voxel size). Non-connected void clusters in the binary specimen were
 452 labelled and then separated into objects (single pores and grains) by using a distance map followed by the
 453 application of a watershed algorithm (e.g., Brabant et al., 2011; Dullien, 2012). Image analysis operations were
 454 assisted by *Fiji-ImageJ software* (Schindelin et al., 2012) and by the *MorphoLibJ plug-in* (Legland et al.,
 455 2014). The following geometrical descriptors were derived from the segmented image limited by the image
 456 resolution of 2.5 μm (Table 1):

- 457 • micro-CT image porosity (IP);
- 458 • Pore specific surface area (PSA – surface to pore volume);
- 459 • Tortuosity: evaluated in the x-, y- and z-directions by finding the average of multiple shortest paths
 460 through the main pore network using the fast marching method (Sethian, 1996) implemented using an
 461 accurate fast marching plug-in in MATLAB.
- 462 • Pore size distribution (PSD): obtained by a Feret maximum calliper (Schmitt et al., 2016).
- 463 • Euler characteristic (χ) - a topological invariant (Wildenschild and Sheppard, 2013; Vogel, 2002) that
 464 describes the structure of a topological space (see Supplementary material for more detail). Since the
 465 number of pore connections depends on the number of grains, (N) , it is essential to normalize χ (Scholz
 466 et al., 2012) to compare the connectivity among three samples that have the same dimensions but

Moved (insertion) [1]

Deleted: 10

Deleted: ,

469 different grain sizes. Thus, a Connectivity Index (CI) parameter, $CI = |\chi|/N$ was defined, where χ and
470 N were computed using image analysis.

Deleted: we defined

471
472 Table 1 allows conducting a comparison between the characteristics derived by the different methods at
473 the different scales of investigation (similarly to Table 1 in Tatomir et al. (2016) that focuses on the similar
474 rock).

Deleted: Connectivity index (CI): computed by dividing the absolute value of the Euler characteristic ($|\chi|$) by the number of grains in the specimen (N , determined by image analysis), $CI = |\chi|/N...$

475 Additionally, we propose a new simple method to estimate the image porosity at a given resolution.
476 Multiplication of the mercury effective saturation at the capillary pressure corresponding to the micro-CT
477 resolution (e.g., 2.5 μm) by the porosity of the same sample measured by a gas porosimeter yields the *micro-*
478 *CT-predicted image porosity from MIP* at the given resolution limit (Table 1).

Deleted: simple and

479
480

487 **4. Results**

488 **4.1. Petrographic and petrophysical rock characteristics**

489 Three types of sandstone rocks were characterized by techniques 1-8 listed in Table 1. The results are
490 presented in Figures 3-8 and summarized in Table 2.

491 **Sandstone S1:** The top unit layer with a thickness of ~1.5 m (Figure 1c) consists of yellow-brown
492 sandstone (Figure 3a), which is moderately consolidated. The sandstone is a mature quartz arenite (following
493 Pettijohn et al., 1987) with minor Fe-ox, feldspar and heavy minerals (e.g., rutile and zirconium). The grain
494 size distribution has a mean of ~325 μm (Figure 6a, Table 2). The grains are moderately sorted (according to
495 the classification of Folk and Ward, 1957) and sub-rounded to well-rounded with local thick (millimetre-scale),
496 relatively dark envelopes (Figure 3b). The sandstone consists of alternating millimetre-scale layers of large
497 and small sand grains. Secondary silt (~45 μm) and clay (~0.95 μm) populations are detected in the grain size
498 distribution (Figure 6). X-ray diffraction detected a small amount of kaolinite. The Fe-ox grain-coating and
499 meniscus-bridging cement is composed of overgrown flakes aggregated into structures ~10 μm in size (Figure
500 3c-3f). Mn oxide is also evident but is scarce (Figure 3e).

501 The pore network is dominated by primary inter-granular well-interconnected macro porosity (Figure
502 3b). However, sealed and unsealed cracks in grains are also observed. Higher Fe-ox cementation at the
503 millimetre scale on horizontal planes is recognized (Figure 3a). In addition, smaller voids between Fe-ox
504 aggregates and flakes occur at the micrometre scale and smaller (Figure 3d-f).

505 The pore throat size analysis conducted with MIP shows that 82 % of the pore volume is composed of
506 macro pores (>10 μm) following a log-normal distribution with a peak at 44 μm (Figure 7a). The characteristic
507 length, i.e., the largest pore throat length at which mercury forms a connected cluster, is $l_c = 42.9 \mu\text{m}$ (Figure
508 7b), and the pore throat length of maximal conductance is $l_{max} = 34.7 \mu\text{m}$ (Figure A1 in Appendix A). The
509 porosity evaluated by laboratory gas porosimetry varies in the range of 26-29 % for 7 different samples of S1
510 (Figure 8). Multiplying the mercury effective saturation (85.8 %) at the micro-CT resolution (2.5 μm) (Figure
511 7a, red dashed line) by the porosity of the same sample measured by gas porosimetry (27.3 %) yields a micro-
512 CT-predicted image porosity of 23.5 % at a resolution limit of 2.5 μm (Table 2).

Deleted:

Deleted: Appendix B,

Deleted: B1

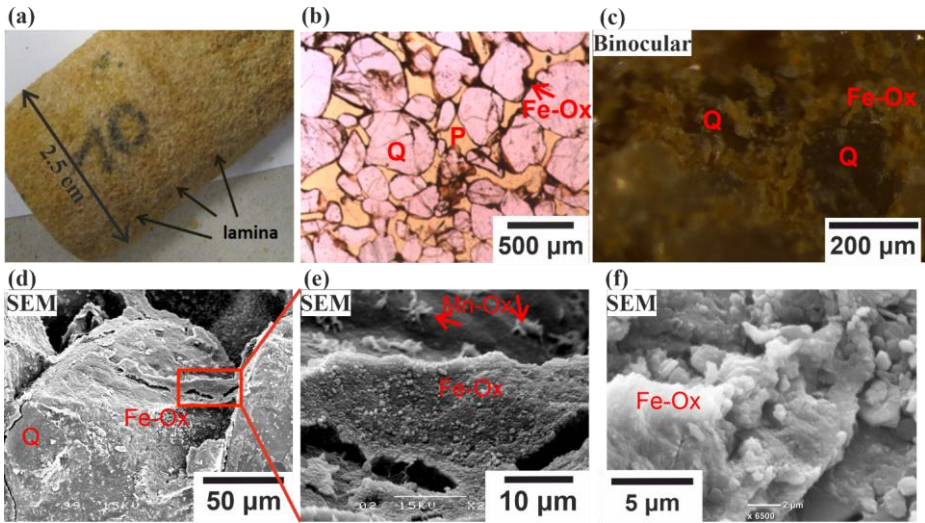
Deleted:

Deleted: s

518 The permeability evaluated by a laboratory gas permeameter has averages of 350 mD (range of 130-
519 500 mD) for 5 samples measured perpendicular to the depositional plane (z-direction) and 640 mD for 2
520 samples measured parallel to the depositional plane (x- and y-directions) (Figure 8). MIP measurement (Katz
521 and Thompson, 1987) yields a permeability (see Sect. 3.2) of 330 mD (Table 2).

Deleted: 350 mD

Deleted: 640 mD



522
523 **Figure 3:** Representative images of sandstone S1. (a) Darker laminae in the x-y plane at the millimetre scale are observed.
524 (b) Thin section image of S1, P refers to open pores, Q – to quartz, Ox to oxide. (c) Fe-ox flakes (yellow) on quartz grains
525 (pale grey). (d) SEM image of S1: grain-coating, meniscus-bridging cement and overgrowth of Fe-ox flakes. (e,f)
526 Magnified images at different scales.

527

528

531 **Table 2.** Petrophysical characteristics of the three studied sandstone layers.

| | Method | S1 | S2 | S3 |
|--|---|--|--|---|
| Grain size | Laser diffraction | 325 µm medium sand moderately sorted sand: 92.6 % silt: 6.6 % clay: 0.8 % | 154 µm very fine sand poorly sorted 65.7 % 31.3 % 3 % | 269 µm fine sand moderately sorted 94.4 % 4.8 % 0.8 % |
| Pore throat size | MIP | Mode 1: 44 µm Mode 2: 0.035 µm Mode 3: 2.2 µm macro pores well sorted | 0.035 µm 3.5 µm meso pores poorly sorted | 35 µm 0.035 µm 2.2 µm macro pores well sorted |
| Pore size | Image analysis (min. object size 2.5 µm) | 194 µm (FWHM [150,335] µm) | Mode 1: 21 µm Mode 2: ~100 µm | 223 µm (FWHM [145,400] µm) |
| Characteristic length, l_c | MIP | 42.9 µm | 12.3 µm | 36.9 µm |
| l_{max} contributing to maximal conductance | MIP | 34.7 µm | 8 µm | 31.4 µm |
| Porosity, ϕ | Gas porosimetry | 28 ± 2 % (7) | 19 ± 5 % (8) | 31 ± 1 % (4) |
| | CT predicted image porosity from MIP | 23.5 % | 6.6 % | 30.4 % |
| | Micro-CT segmented | 17.5 % | 6.9 % | 28.3 % |
| Permeability, κ ⊥ - perpendicular to layering (z-direction) - parallel to layering (x-y plane) | Gas permeametry | ⊥ 350 mD (5) 640 mD (2) | ⊥ 2.77 mD (5) 7.73 mD (3) | ⊥ 220* mD (2) 4600* mD (2) |
| | MIP | 330 mD (1) | 4 mD (1) | 466 mD (3) |
| | Flow modelling | $\begin{pmatrix} 420 & 66.3 & 1.91 \\ 66.3 & 344 & 12.8 \\ 1.91 & 12.8 & 163 \end{pmatrix}$ mD | - | $\begin{pmatrix} 4517 & 5 & 38 \\ 5 & 4808 & 547 \\ 38 & 547 & 4085 \end{pmatrix}$ mD |
| Specific surface area, SSA (surface-to- bulk-volume) | MIP | 3.2 µm ⁻¹ | 12.2 µm ⁻¹ | 0.16 µm ⁻¹ |
| Pore specific surface area, PSA (surface-to-pore-volume) | Micro-CT at 2.5 µm resolution size | 0.068 µm ⁻¹ | 0.136 µm ⁻¹ | 0.069 µm ⁻¹ |
| Connectivity index | Image analysis | 3.49 | 0.94 | 10 |
| Tortuosity, τ | Flow modelling | - | - | x: 1.443 y: 1.393 z: 1.468 |
| | Micro-CT shortest path analysis | x: 1.385 y: 1.373 z: 1.477 | - | x: 1.316 y: 1.338 z: 1.394 |

Deleted: *

Deleted: *

Deleted: **

532 Legend:

536 Numbers in parentheses related to gas porosity, gas permeability and MIP permeability, indicate the number
537 of plugs for the measurements. Other measurements and calculations were conducted on single plugs.
538 FWHM - full width at half maximum, log-normal distribution.

Deleted: *Addressed in the Discussion.
**

539
540 **Sandstone S2:** The intermediate unit layer with a thickness of ~20 cm consists of grey-green moderately
541 consolidated sandstone (Figures 1c, 4) composed of sub-rounded to rounded, very fine sand grains (~154 μm);
542 the sandstone is poorly sorted with 35 % of the particles being silt and clay (Figure 6, Table 2). Secondary silt
543 (~ 40 μm), sand (~400 μm) and clay (~1.5 μm) populations are also detected. The grains are composed of
544 quartz with minor Fe-ox coating the grains and minor quantities of heavy minerals (e.g., rutile and zirconium)
545 (Figure 4c). Clay filling the pore space was identified by XRD as a kaolinite mineral. It appears as a grain-
546 coating, meniscus-bridging, and pore-filling matrix (Figure 4b, c). Therefore, the unit layer (Figure 1c) is
547 classified as a quartz wacke sandstone (Pettijohn et al., 1987).

Deleted: .

Deleted: consists

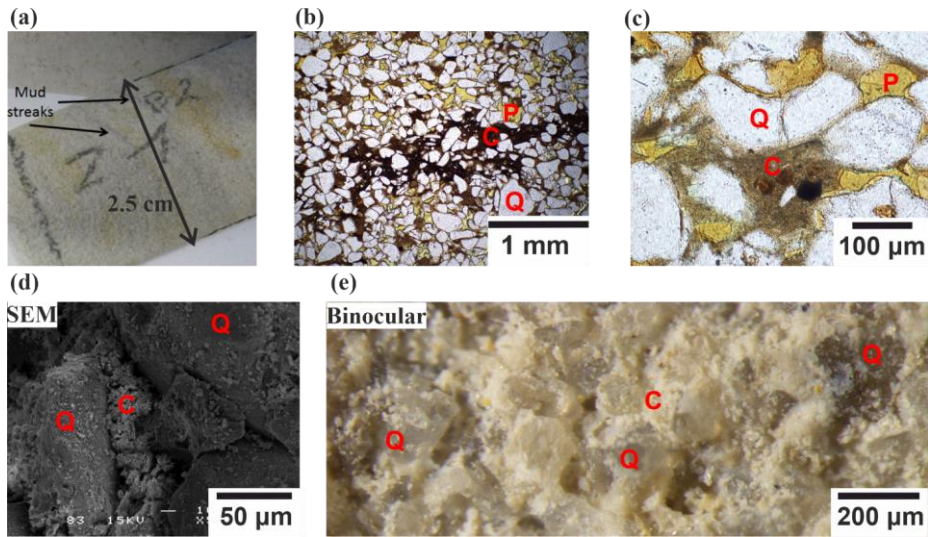
548 The pore space is reduced by clays deposited on coarser grains, identified mostly in laminae (Figure 4a,
549 d). However, the inter-granular connectivity of macro pores can still be recognized (Figure 4b, c). The
550 effective pore network consists of inter-granular macro pores distributed between the laminae or zones richer
551 in clay and Fe-ox. Integrating the grain size and pore throat size analysis results (Figs. 6, 7) confirms that the
552 reduction in the inter-granular pore space in S2 is due to the clay matrix, which is reflected in the poor grain
553 sorting and large variance in pore size. In the pore throat size analysis (Figure 7), only 15 % of the pore volume
554 is composed of macro pores that are larger than 10 μm . The prominent sub-micron pore mode is ~35 nm, with
555 a population containing ~45 % of the pore volume (Figure 7a). This population of pores occurs inside the clay
556 matrix. The secondary pore volume population is poorly distributed within the range of 0.8-30 μm . The
557 characteristic length (Sect. 3.2), $l_c = 12.3 \mu\text{m}$ (Figure 7b), and the pore throat length of maximal
558 conductance, $l_{max} = 8 \mu\text{m}$ (Figure A1 in Appendix A) (both lengths have large analytical uncertainties,
559 resulting from uncertainty in the threshold pressure, cyan colour in Figure 7b), suggest a connectivity of macro
560 pores regardless of their small fraction within the total pore space. The porosity of S2 evaluated for 8 different
561 samples varies in the range of 14.5-23.5 % (Figure 8). From the PTSD (Table 1) and gas porosimetry results
562 (for a sample with a porosity of 18.6 %), micro-CT predicts an image porosity of 6.6 % at a resolution limit
563 of 2.5 μm (Table 2). The gas permeability in the z-direction was measured in 5 samples (Figure 8): in four of
564 them, the permeability ranges within 1-12 mD and increases with porosity. However, one sample had an

Deleted: Appendix B, Figure B1

Deleted: a

Deleted: y

572 exceptionally large porosity and permeability of 23 % and 62 mD, respectively. The permeability measured
573 for 3 samples in the x-y plane ranges within 4-12 mD, also showing ~15 % porosity (Figure 8). In addition,
574 samples with ~15 % porosity, have permeability values larger in the x-y plane (parallel to the layering) than
575 in the z-direction (perpendicular to the layering). The permeability derived from MIP reaches 4 mD, which
576 agrees with an average of 2.77 mD and 7.73 mD (Table 2) measured in the z-direction with a gas permeameter
577 (excluding one exceptionally high value, Figure 8).



578
579 **Figure 4.** Representative images of sandstone S2. (a) Dark stains in the rock are mud streaks, yellowish zones are due to
580 increased Fe-Ox cement. (b) The dark laminae are richer in clays and Fe-ox. P refers to open pores, Q – to quartz, C –
581 to clay. (c) Clay and silt accumulated as meniscus and as clay matrix. (d) Pore clogged by clay and Fe-ox. (e) Rock
582 texture. The clay matrix is white, and quartz grains are pale grey.

583

584 **Sandstone S3:** The bottom unit layer with a thickness of ~1.5 m consists of (pale) red-purple poorly
585 consolidated sandstone (Figure 1c) with grains covered by a secondary red patina (Figure 5). The sandstone
586 is composed of friable to semi-consolidated, fine (~269 µm), moderately sorted sand (Table 2), where only
587 5.6 % of particles are silt and clay (Figure 6). Secondary silt (~ 50 µm) and clay (~ 0.96 µm) populations were

Deleted: for the

Deleted: .

Deleted: their

Deleted: is

Deleted: ten times

593 also detected. The sandstone consists of sub-rounded to rounded grains showing a laminated sedimentary
594 texture consisting of the cyclic alternation of relatively dark and light red bands of millimetre-scale thickness
595 (Figure 5a). The dark laminae contain slightly more Fe-ox meniscus-bridging and pore-filling cementation
596 (Figure 5b, d). Overall, this bed consists of a ferruginous quartz arenite. The grains are dominated by quartz
597 with very minor feldspar and black opaque mineral grains, perhaps Fe-ox (Figure 5d). X-ray diffraction
598 indicated quartz only. The Fe-ox coating of grains is less extensive than in other samples (Figure 5c). The
599 pore interconnectivity in this sandstone is high (Figure 5d). Heavier cementation is rarely observed (Figure
600 5d) and is organized in horizontal laminae (Figure 5a). Features including grain cracks, grain-to-grain
601 interpenetration, and pressure solution are also recognized (Figure 5e). The *PTSD* showed that 95 % of the
602 pore volume is presented by macro pores (Figure 7a), which agrees with the [scarcity](#) of fine particles. The
603 characteristic length and pore throat length of maximal conductance are $l_c = 36.9 \mu\text{m}$ (Figure 7b) and $l_{max} =$
604 $31.4 \mu\text{m}$ ([Figure A1 in Appendix A](#)), respectively.

605 The porosity measured by a gas porosimeter in the laboratory varies in the range of 30-32 % for 4
606 different samples (Figure 8). From *PTSD* and gas porosimetry ([Figures 7, 8](#)), the micro-CT-predicted image
607 porosity at a resolution limit of $2.5 \mu\text{m}$ is 30.4 % (Table 2). The permeability measured by a laboratory gas
608 permeameter averages 220 mD for 2 samples measured in the z-direction and 4600 mD for 2 samples
609 measured in the x-y plane (Figure 8), showing a ten-fold difference (discussed in Sect. 5). The permeability
610 derived from MIP reaches 466 mD (Table 2).

Deleted: minority

Deleted: Appendix B, Figure B1

Deleted: .

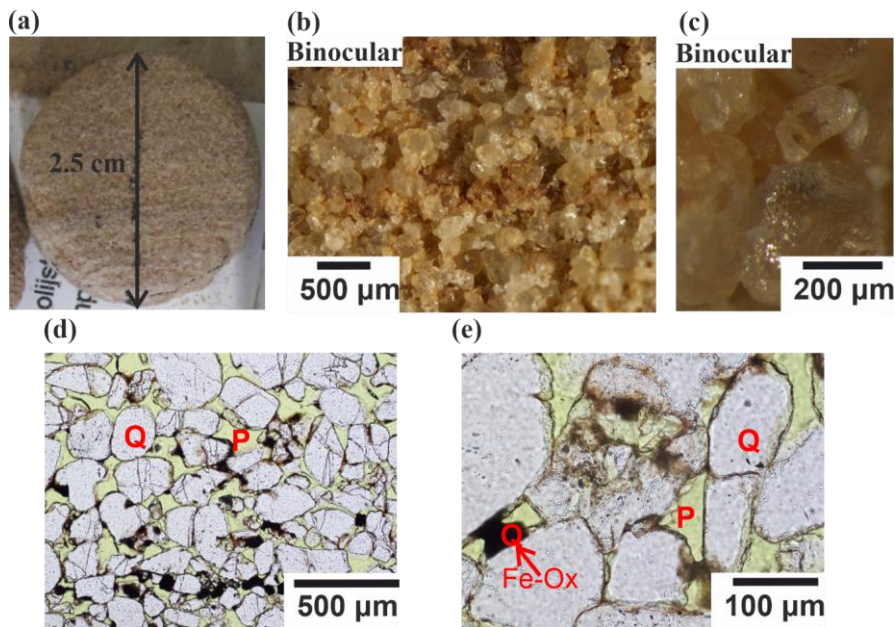
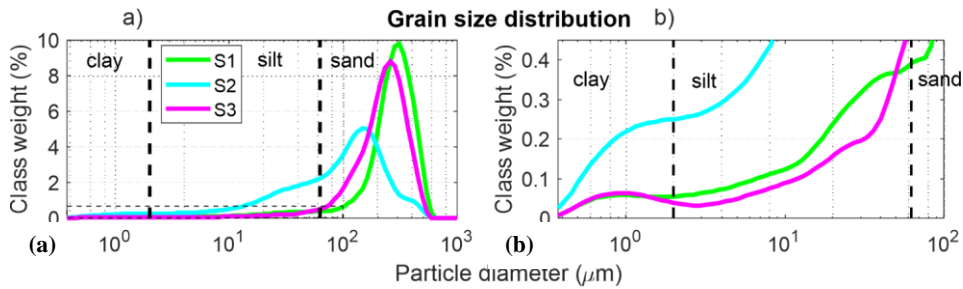


Figure 5. Representative images of sandstone S3. (a) Laminae are recognized by their slightly dark and red colour. (b) General view reveals red laminae ~300 μm thick. (c) High-resolution observation of a clear grain. (d) A millimetre-scale lamina is indicated by enhanced meniscus-type Fe-ox cementation and partly by inter-granular fill. Grain surfaces are coated by thin Fe-ox. Black and orange cements represent crystallized and non-crystallized Fe-ox, respectively. Some cracked grains are observed, sporadically cemented by Fe-ox. P refers to open pores, Q – to quartz. (e) Partially dissolved grains are coated by cement.

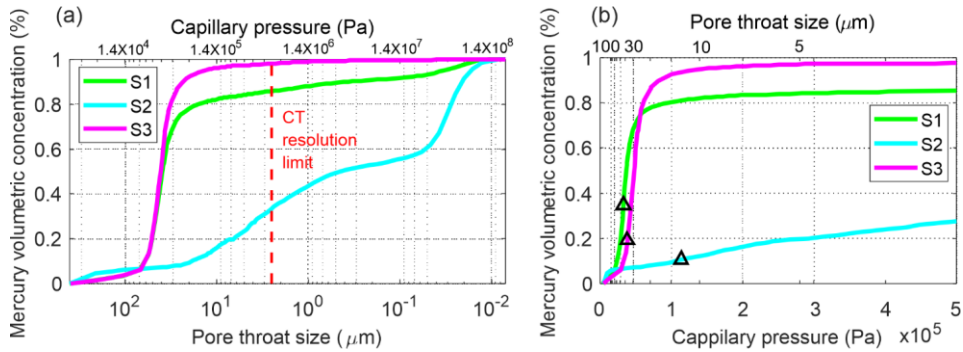
623



624

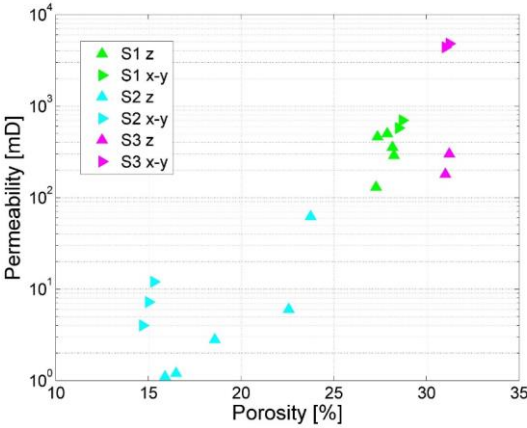
625 **Figure 6:** (a) Grain size distribution. (b) Magnified grain size distribution in the fine grain size region plotted
 626 for sandstones S1 (green), S2 (blue) and S3 (purple). S1 and S3 have a unimodal distribution and are
 627 moderately sorted with a small skewness tail. Sample S2 has a multi-modal distribution and is poorly sorted.

628



629 **Figure 7:** Cumulative pore throat sizes of the studied sandstones. (a) Capillary pressure on a logarithmic
 630 scale. The resolution limit of the micro-CT imaging indicates the fraction of the pore space that could be
 631 resolved. (b) Capillary pressure on a linear scale. The triangles indicate the characteristic length, l_c .

632



633

634 **Figure 8:** Results of porosity-permeability lab measurements. The permeability of the samples was measured
635 in directions perpendicular to the bedding (z-direction) and parallel to the bedding (x-y plane).

636 Overall, the relative decrease in l_{max} with respect to l_c is greater for the layers containing more fines
637 (Table 2).

638 Additionally, pore surface roughness may be evaluated from the specific surface area (SSA) measured
639 by MIP (Table 2). A larger SSA implies a rougher surface (e.g., Tatomir et al., 2016). The SSAs for S1 and S2
640 ($3.2 \mu\text{m}^{-1}$ and $12.2 \mu\text{m}^{-1}$, respectively) are similar to those given in the literature for sandstones of similar
641 properties (e.g., Cerepi et al., 2002). The SSA of S2 is higher because of its high silt and clay content of 34.3
642 %, which is only 7.4 % for S1 (Figure 6a). The SSA of S3 (where silt and clay constitute only 5.6 %, including
643 the Fe-ox rim coating) is only $0.16 \mu\text{m}^{-1}$, which is 20 times smaller than that of S1 (Table 2). The difference
644 in SSAs between S1 and S3, which are similar in their grain and pore throat size distributions (Figs. 6, 7), is a
645 result of S1 having a higher Fe-Ox grain coating than S3 (compare Figures 3d and 5c).

Deleted: for all three investigated sandstones, the pore throat size contributing to the maximal conductance, l_{max} , is smaller than the characteristic length, l_c (Table 2), when
Deleted: with relation

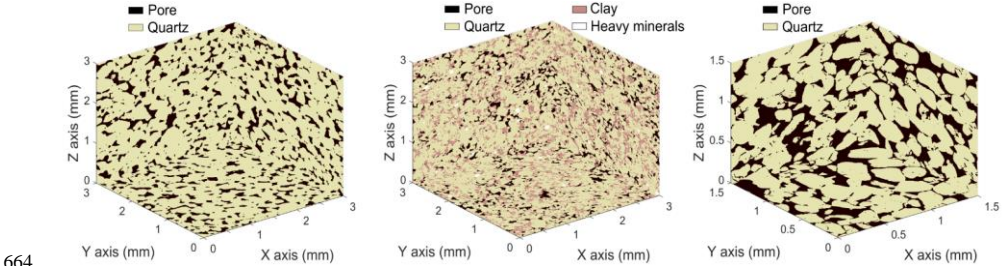
Deleted: .

651 In summary, although the S1 pore network has larger pore throats, it also has greater grain roughness
652 and lower connectivity than S3. These two properties dominate and generate a smaller permeability for S1
653 than for S3 (Table 2).

654 **4.2. Image analysis**

655 Visualized segmented sub-volumes of samples S1, S2, and S3, depicting [quartz](#), pores, clay and heavy
656 minerals, are presented in Figure 9. The main pore size population in PSD of S1 is at ~100-500 μm range with
657 majority at ~194 μm (Figure 10). A smaller population of pores of ~30-100 μm was identified as well, which
658 may refer to (Mode 1) pore throat size derived from the MIP experiment (Table 2). Image resolution of 2.5
659 μm limited the analysis. The pore specific surface area (PSA) calculated from micro-CT images is
660 $0.068 \mu\text{m}^{-1}$. The tortuosity, measured from the whole CT image, indicates similar values in the x- and y-
661 directions of 1.37 and 1.38, respectively, whereas in the z-direction, the tortuosity is 1.48 (Table 2). As many
662 paths were considered, this difference indicates the textural features that appear in horizontal plane (Figure
663 3a).

Deleted: Quartz



665 **Figure 9:** Visualized [in these pictures](#) sub-volumes of segmented CT samples of (a) S1, (b) S2, (c) S3. S1 and
666 S2 in this visualization have volumes 3^3 mm^3 scanned with $5 \mu\text{m}$ voxel size resolution, S3 has volume 1.5^3 mm^3
667 scanned with $2.5 \mu\text{m}$ voxel size.

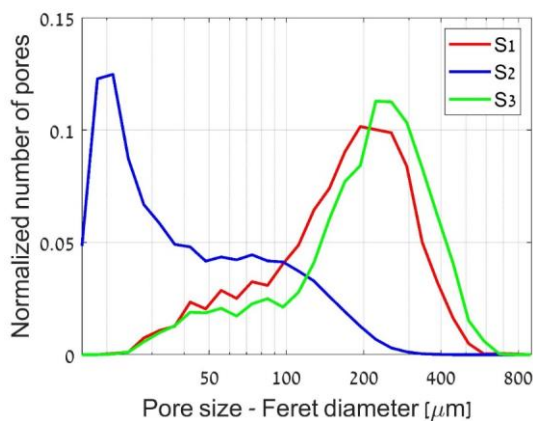


Figure 10: Statistics of the pore sizes calculated by image analysis for three sandstone samples: S1, S2, and S3. Number of pores analysed: S1 – 3500, S2 – 45000, S3 – 3500. The CT data sets used for this analysis had 2.5 μm voxel size resolution to capture grain and pore shapes better, compared to those at resolution of 5 μm .

For S2 (Figure 9), the main pore size population is in the $\sim 15\text{--}50\text{ }\mu\text{m}$ range (Figure 10), with majority at $\sim 21\text{ }\mu\text{m}$. This may refer to the pore throat size derived from MIP. However, smaller pore throat sizes which were derived from the MIP (mode peak is at $\sim 3.5\text{ }\mu\text{m}$) could not be visualized due to the limited resolution of the image ($2.5\text{ }\mu\text{m}$), and because of high uncertainty associated with size of pores smaller than $10\text{ }\mu\text{m}$ (four voxels). Accordingly, they were excluded from the PSD evaluation (Figure 10). A large pore population is also recognized at $\sim 100\text{ }\mu\text{m}$ (Figure 10), which corresponds to the pore size scale recognized from the petrography (Figure 4), MIP (Figure 7) and CT image (Figure 9). The pore specific surface area (PSA) calculated from micro-CT images is $0.136\text{ }\mu\text{m}^{-1}$ (Table 2), which is twice as large as the PSA of S1.

For S3 (Figure 9), the main pore size population is in the $\sim 100\text{--}500\text{ }\mu\text{m}$ range (Figure 10), with majority at $\sim 223\text{ }\mu\text{m}$. The geometry-based tortuosity values measured from the whole CT image with multiple paths is 1.32, 1.34 and 1.39 in the x-, y- and z-directions, respectively. The tortuosity is lower for S3 than for S1 in all directions, which is a direct result of the smaller amount of cement in the pore throats. The PSA of S3 is $0.069\text{ }\mu\text{m}^{-1}$, which is similar to that of S1.

Deleted: samples

Deleted: .

Deleted: at

Deleted: (

Deleted: at

Deleted: .

Deleted: at

693 4.3 REV Analysis

694 4.3.1. Quartz arenite sandstones (S1 and S3)

695 One-dimensional profiles of porosity of S1 (Figure 11(a-c)) were evaluated by averaging the pore
696 voxels over each slice in sequential slices in three orthogonal directions (hereafter referred as slice-by-slice
697 porosity). The investigated domain had a volume of $6.8 \times 6.9 \times 9.2 \text{ mm}^3$ scanned with a voxel size of $5 \text{ }\mu\text{m}$
698 (suitable for imaging pore throats that effectively contribute to the flow in S1, Table 2). The slice-by-slice
699 porosity distinguishes the z-direction as having an exceptional behaviour, with variance in porosity
700 fluctuations being four times larger than that in x- and y- directions (i.e., 0.98 in z- direction, compared to 0.17
701 and 0.16 in the x- and y- directions, respectively). Porosity fluctuates with peak to trough length of ~0.1 mm
702 in x- and y- directions that could refer to an average pore cross-section over the slice, and thus being attributed
703 to grain packing. In z- direction an additional larger scale wavelength of ~3.5 mm is observed, where peaks
704 and troughs could refer to higher and lower porosity layers, respectively, thus being attributed to depositional
705 processes.

- Deleted: osity
- Deleted: in
- Deleted: a
- Deleted: in
- Deleted: over
- Deleted: of S1,
- Deleted: having a maximal available segmented
- Deleted: investigated
- Deleted: was
- Deleted: .
- Deleted: around the mean value
- Deleted: a wavelengths
- Deleted: 2
- Deleted: and grain
- Deleted: related
- Deleted: but also with
- Deleted:
- Deleted: (observed in z- direction only)
- Deleted: related
- Deleted: that may be attributed to combined width of two higher and lower millimetre-scale layers..

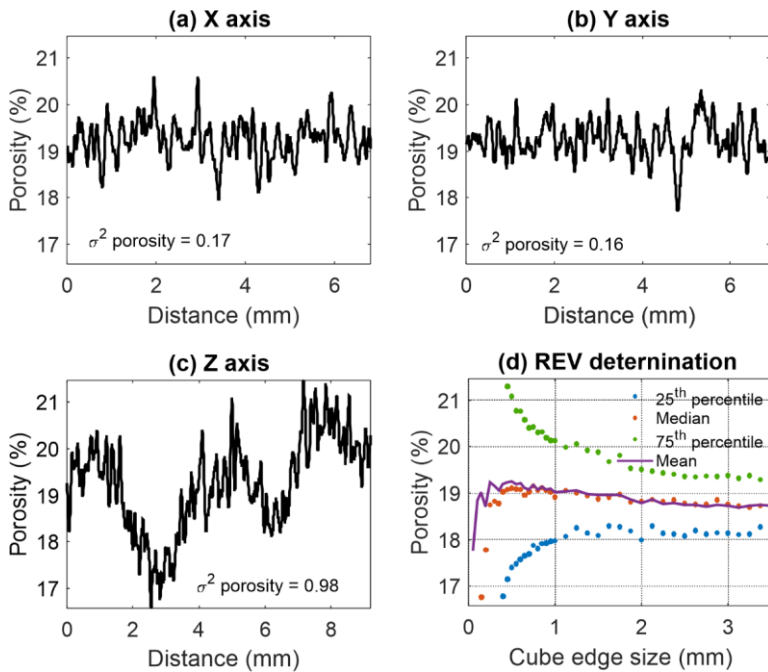


Figure 11: Determination of REV in S1. a) One-dimensional porosity profile of S1 slices evaluated in a) x-direction, b) y-direction and c) z-direction. (d) Classic REV analysis. Investigated volume size is $6.8 \times 6.9 \times 9.2 \text{ mm}^3$.

Alternatively, the REV size was estimated as $\sim 2.5 \text{ mm}$ (Figures 11d) by classic REV analysis, where the mean, median, 25th and 75th percentile porosity changes decline. Considering these results (Figure 11), we decided to use a segmented specimen cube with a maximal available edge length of $2950 \mu\text{m}$, scanned with a higher resolution of $2.5 \mu\text{m}$ (to preserve the grain surface geometry and a consistency between S1 and S3 samples) for flow simulations.

One-dimensional profiles of slice-by-slice porosity were evaluated in sequential slices in the orthogonal directions of S3 with a maximal segmented volume of $3 \times 3 \times 4.2 \text{ mm}^3$ scanned with a voxel size of $2.5 \mu\text{m}$

Deleted: al

Deleted: 1.2

Deleted: A1a, b

Deleted: Therefore, c

Deleted: of

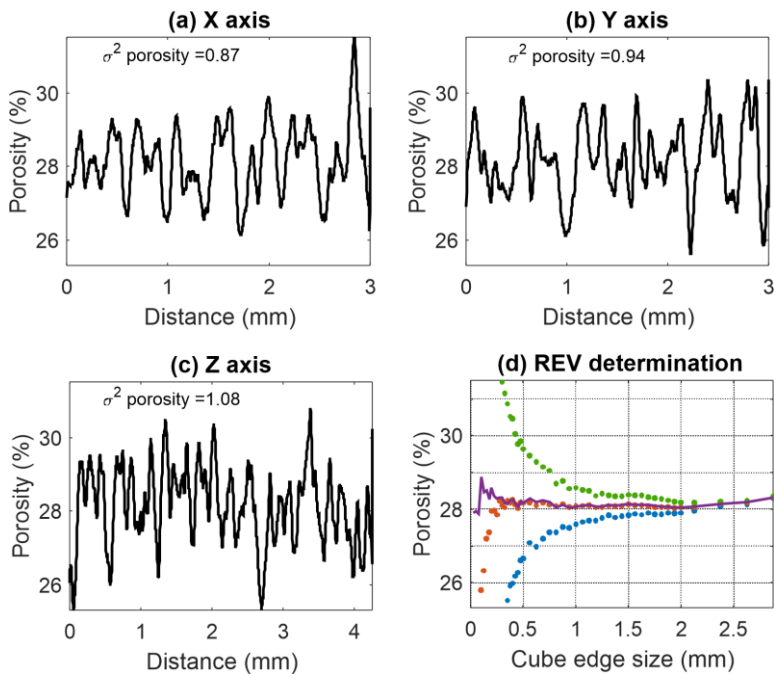
Deleted: to preservethe grain surface geometry

Deleted: ,

Deleted: ,and

Deleted: However, for sub-volumes larger than 3.8 mm the median decreases compared to the mean porosity, which may refer about sub-volumes which include more large pores, which are related to the more porous layers that were implied from Figure 11c.

750 (Figures 12a-c). Porosity fluctuates in all directions with peak to trough distance of ~0.1 mm that could refer
751 to an average pore cross-section over the slice, as clarified for S1. The variance is similar in all directions
752 (0.87, 0.94, 1.08, correspondingly) that implies a homogenous sample. REV with an edge length of 875 μm
753 was estimated by classic analysis (Figure 12d), which was used for the flow simulation in S3.



757 **Figure 12:** Determination of REV in S3. a) One-dimensional porosity profile of S3 slices evaluated in a) x-
758 direction, b) y-direction and c) z-direction. (d) Classic REV analysis. Investigated volume size is $3 \times 3 \times 4.2$
759 mm^3 .

- Deleted: 13a
- Deleted: around the mean with no trend
- Deleted: ns with a
- Deleted: wavelength
- Deleted: length
- Deleted: .
- Deleted: explained
- Deleted: on
- Deleted: .
- Deleted: Classic
- Deleted: porosity
- Deleted: analysis
- Deleted: was estimated (Appendix A, Figure A1e, f)
- Deleted: yields REV size with
- Deleted: for
- Deleted:
- Deleted: cube
- Deleted: sub-volume
- Deleted: which is about ten-fold larger than the ranges observed in the semivariogram analysis (~0.1 mm, which is a typical size of a pore). For the same reasons used in estimations of REV by the classic approach in S1,
- Deleted: the classic REV derived
- Deleted: volume
- Deleted: modelling

- Deleted: 3
- Deleted: al

787 4.3.2. Quartz wacke sandstone (S2)

788 Sample S2 is more heterogeneous than S1 and S3 because of the deposition of clay in a patchy
789 distribution. The sample is visualized in Figure 9b with quartz grains (yellow), pore volume (black), clay
790 matrix (brown) and heavy minerals (white). In Figure 13a-c, the porosity of sequential slices in the orthogonal
791 directions is shown together with clay matrix content, evaluated in segmented volume of $7.9 \times 6.8 \times 9.2 \text{ mm}^3$
792 size scanned with a voxel size of $5 \text{ }\mu\text{m}$. In z-direction a clear trend in porosity is observed, which has a negative
793 correlation with the clay content (Figure 13f), whereas in the horizontal (x-y) plane there is no clear correlation
794 (Figure 13d-e). This correlation in z- direction implies that the porosity is controlled by depositional processes.
795 However, the similar large-scale wavy structures of the clay content in x- and y- directions (Figures 13a, b)
796 may refer to errors originated from the scanning and inversion in the CT acquisition, as x- and y-coordinates
797 are associated with the side boundaries of the cylindrical sample

Deleted: The clay matrix is distributed in patches.

Deleted: 5

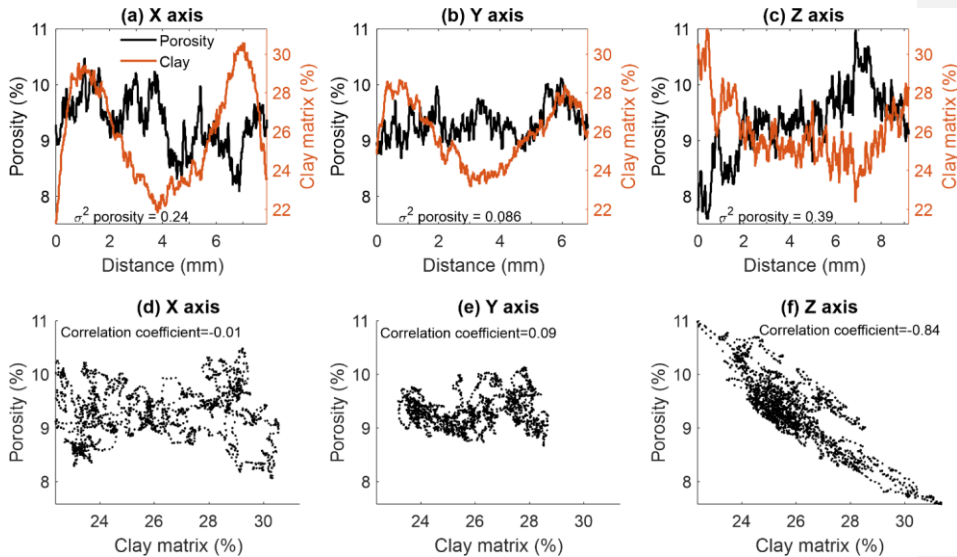
Deleted: planes

Deleted: 16

Deleted: the

Deleted: (

Deleted: 15a



798

799 **Figure 13:** Correlation between porosity and clay. Porosity and clay profiles (left and right y-axes,
800 correspondingly) in slices of S2 evaluated in (a) x-direction, (b) y-direction (c) z-direction. Scatterplots of clay

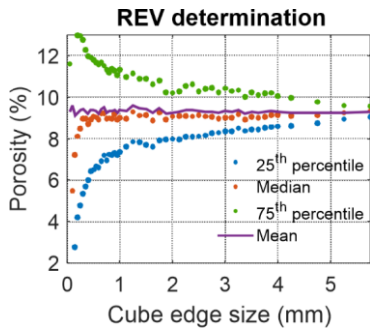
Deleted: 5

Deleted: (left)

Deleted: (right)

811 content and porosity in S2 in (d) x-direction, (e) y-direction, (f) z-direction.) Investigated maximal segmented
812 volume size is $7.9 \times 6.8 \times 9.2 \text{ mm}^3$ (see text for more detail).

813



814

815 Figure 14: Classic REV analysis of S2. Investigated volume size is $7.9 \times 6.8 \times 9.2 \text{ mm}^3$.
816 Classic REV evaluation (Figure 14d) may indicate a cube edge size of $\sim 3 \text{ mm}$. However, the porosity
817 trend in z-direction (Figure 13c) in the volume under investigation, implies that, no REV can be found in S2
818 sample. As a result, flow modelling could not be conducted in sample S2.

819 4.4. Flow modelling at the pore scale

820 Fluid flow was modelled at the pore scale in two different micro-CT-scanned geometries: 1) a full cube
821 of sample S1, and 2) sample S3 within its REV dimensions (Table 3), imaged with $2.5 \mu\text{m}$ voxel size.
822 Modelling of the 3D geometry of sample S2 was not performed due to its non-stationarity, which did not allow
823 finding the REV in the investigated domain.

824 Table 3. Porosity losses in S1 and S3 over the course of applying the extended computational workflow (Figure
825 2).

| Sample | Sample size (mean mesh edge size) [μm] | CT segmented image porosity (%) | Connected porosity (%) | Mesh porosity (%) | Gas porosity (%) |
|------------------------------------|--|------------------------------------|---------------------------|----------------------|---------------------|
| S1 (entire sample, 1180 voxels) | 2950 (14) | 17.5 | 15.6 | 13.6 | 28 |
| S3 (REV, 350 voxels) | 875 (5) | 28.3 | 27.9 | 25.9 | 31 |

Deleted: r

Deleted: al

Deleted: Additionally/alternatively, the large difference between the mean and median porosities is identified by the classic porosity-based ...

Deleted: al

Deleted: approach

Deleted: Appendix A,

Deleted: 7

Deleted: A1c,

Deleted: on REV

Deleted: Together with

Deleted: 15

Deleted: ($7.9 \times 6.8 \times 9.2 \text{ m}^3$)

Deleted: this

Deleted: there is

842

843 The porosity of the meshed domain of sample S1 is 13.6 % (in contrast to 17.5 % in the segmented
844 image, Table 3), and the mesh edge length is 14 μm along the pore walls. The observed porosity loss results
845 from disconnecting narrow pore throats from the connected cluster imaged with a 2.5 μm voxel size due to
846 the use of a 14 μm mesh size (the lowest possible for our computational needs). A maximum Reynolds number
847 of $Re = 0.084$ was used to guarantee the simulation in a creeping flow regime.

848 The symmetrized permeability tensor, $\bar{\kappa}$ (Eq.5), was obtained as follows (Table 2):

849
$$\bar{\kappa}_{sym} = \begin{pmatrix} 420 & 66.3 & 1.91 \\ 66.3 & 344 & 12.8 \\ 1.91 & 12.8 & 163 \end{pmatrix} \quad (6)$$

850

851 The permeability tensor is anisotropic, with κ_{zz} being more than twice smaller than κ_{xx} and κ_{yy} . This
852 result is in agreement with the appearance of horizontal banding with higher cementation (Figure 3a).

853 The porosity of the meshed domain of sample S3 is 25.9 % (in contrast to 28.3 % in the segmented
854 image, Table 3), and the mesh edge length is 5 μm along the pore walls. A maximum Reynolds number of
855 $Re = 0.22$ was used to guarantee the simulation in a creeping flow regime. The symmetrized permeability
856 tensor is close to isotropic (Table 2):

857
$$\bar{\kappa}_{sym} = \begin{pmatrix} 4517 & 5 & 38 \\ 5 & 4808 & 547 \\ 38 & 547 & 4085 \end{pmatrix} \quad (7)$$

858 Additional permeability tensor simulations on equivalently REV sized segmented sub-volumes of S3
859 and on the full S3 (Figure 15, cube volume of $3 \times 3 \times 3 \text{ mm}^3$) have been performed with GeoDict toolbox, to
860 ensure consistency of the estimated REV size. Sub-volumes locations are presented. Symmetrized
861 permeability tensors simulated in these domains (Figure 16) are close to the former one (Eq. 7) being also
862 nearly isotropic.

Deleted:

Deleted: half

Deleted: derived from the semivariogram analysis (Figure 11c).

Deleted: 7

Deleted: 8

Deleted:

Deleted: 9

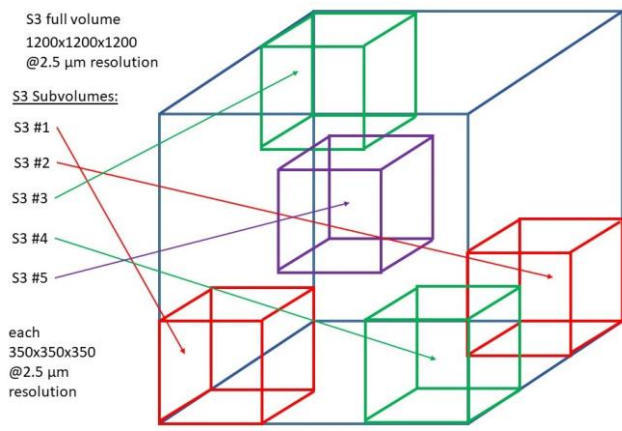


Figure 15: Selection of the sub-volumes in the S3 CT dataset, for additional permeability tensor simulations.

Each sub-volume has a size of 350 voxels cubed, while full volume is of 1200 voxels cubed size.

Deleted: 8

Deleted: of

Deleted: modelling

Deleted: domain

| | | | | | | | | | |
|---------|------|------|------|--------------------------------------|-------|------|------|------|--------------------------------------|
| S3_full | 4247 | 98 | 117 | avg. k: ~4500 mD $\phi = 26.88\%$ | S3_#3 | 5032 | 5 | 6 | avg. k: ~4799 mD $\phi = 27.33\%$ |
| | 98 | 4820 | 483 | | | 5 | 4143 | 10 | |
| | 117 | 483 | 4432 | | | 6 | 10 | 5223 | |
| S3_#1 | 5485 | 125 | 4 | avg. k: ~5290 mD $\phi = 27.47\%$ | S3_#4 | 4601 | 4 | 4 | avg. k: ~3915 mD $\phi = 26.75\%$ |
| | 125 | 5882 | 2 | | | 4 | 3799 | 5 | |
| | 4 | 2 | 4504 | | | 4 | 5 | 3344 | |
| S3_#2 | 4392 | 122 | 4 | avg. k: ~3754 mD $\phi = 25.99\%$ | S3_#5 | 4397 | 10 | 70 | avg. k: ~4027 mD $\phi = 27.53\%$ |
| | 122 | 3510 | 185 | | | 10 | 3825 | 6 | |
| | 4 | 185 | 3359 | | | 70 | 6 | 3858 | |

In sub-samples: avg. k: 4381 mD / median k: 4522 mD

Figure 16: Permeability tensor simulation results and evaluated 3D image porosity data for the sub-volumes and full sample S3 specified in Figure 15.

The tortuosity of S3 computed from particle tracing in the x-, y-, and z- directions is 1.44, 1.39 and 1.47, correspondingly (Table 2). The largest value is observed in the z-direction, which is in agreement with the lowest permeability in the z-direction.

5. Discussion

5.1. Validation of permeability by micro- and macro-scale rock descriptors

Each of the evaluated micro- and macro-scale rock descriptors supplies a qualitative information about the sample permeability (Tables 2-3), which is used to validate the multi-methodological approach presented in this paper. Specifically, the increasing mercury effective saturation with increasing pressure shows a similar pore throat size distribution curve slope for sandstone samples S1 and S3 in the macro-pore throat range (Figure 7), suggesting that these samples have similar structural connectivity. However, S1 has a smaller imaged volume fraction of pore space available for fluid flow that is controlled by macro pore throats (i.e., 81

Deleted: 9

Deleted: varies in the range [1.39, 1.47]

Deleted: x

Deleted: y

Deleted: z

Deleted: ,

Deleted: and t

909 % in S1 vs. 93 % in S3, Figure7) due to its higher contents of silt, clay, and Fe-ox cement. The intermediate
910 layer (S2) with 19 % porosity comprises more fines, which form a clay matrix (Table 2) due to poor grain
911 sorting and smaller mechanical resistance of clay to pressure under the burial conditions. Only ~15 % of the
912 pore volume fraction in S2 is controlled by bottle-neck macro pore throats (Figure 7). However, the
913 characteristic length of S2, 12.3 μm (Table 2), indicates that macro-pore connectivity is still possible even
914 when the pore space consists mainly of sub-macro-scale porosity. This 0.15 volume fraction is in agreement
915 with Harter (2005), who estimated a volume fraction threshold of 0.13 for correlated yet random 3D fields
916 required for full interconnectivity.

917 The value of the connectivity index of S3 (10) ~~evaluated from CT data~~ is approximately three times higher
918 than that of S1 (3.49), while both rocks are defined as moderately sorted sandstones (Table 2). This difference
919 is due to S1 having a smaller number of inequivalent loops within the imaged pore network than S3, leading
920 to smaller Euler characteristics (see Supplementary material for more detail). Inequivalent loops are positively
921 correlated with pore throats; their number is affected by the resolution of the CT image and by the partial
922 volume effect at grain surfaces (Cnudde and Boone, 2013; Kerckhofs et al., 2008), where some voxels could
923 be identified as grains and thus “clog” the small pore throats. Artefact porosity loss is apparent for S1, where
924 the IP is 17.5 % (in contrast to the CT porosity of 23.5 % predicted from MIP, Table 2). The connectivity
925 index of S2 (0.94, Table 2) is lower than those of both S1 and S3 because of the clay matrix, which clogs
926 pores with sizes below the image resolution. The effect of the partial volume effect on the image connectivity
927 and on the preservation of small features was reviewed by Schlüter et al. (2014).

928 A correlation was found between the grain size and the amount of Fe-ox cement in S1 evaluated at each
929 slice along the z-direction (from the image analysis, Figure 17). Exceptionally large grains are detected
930 (indicated by the red rectangle) near the cemented region at ~750 μm . Large grains and a relatively high
931 amount of cement can also be observed in the S1 thin section (Figure 3b). Large grains cause large pores and
932 generate relatively permeable horizons through which water flow and solute transport can become focused
933 (McKay et al., 1995; Clavaud et al., 2008), supplying iron solutes. We suggest that a vadose zone was formed
934 after flooding events, where the water flow mechanism could have changed from gravity dominated to
935 capillary dominated. Water then flowed due to capillary forces along grain surfaces towards regions with
936 larger surface areas, and iron solutes precipitated in a reaction with oxygen available in the partly saturated
937 zone. We suggest that with time, this cementation mechanism caused a decrease in the pore throat size near

Deleted: computed

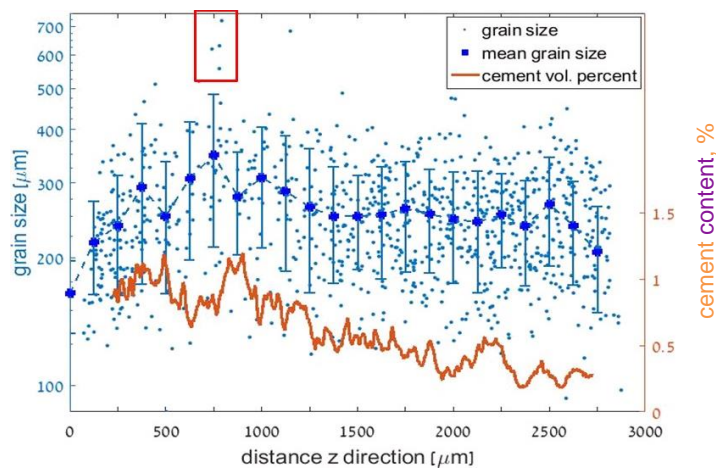
Deleted: based on

Deleted: β_i

Deleted: s values in

Deleted: 20

943 the preferential path, while the preferential path with a low surface area remained open, eventually generating
944 the observed anisotropic flow pattern.



946 **Figure 17.** Grain size scattering and Fe-ox cement content in sandstone S1 in slices along the z-direction. The
947 red rectangle emphasizes very large grains that were detected.

948 In this respect, permeability anisotropy in sandstones at a small scale is usually attributed to the shape or
949 preferential orientation of grains and pores (e.g., Sato et al., 2019) and to a heterogeneous distribution of
950 cementing material at grain contacts (Louis et al., 2005). Clay-free and cement-free layers in S1 thus constitute
951 the main avenues for flow in the parallel direction, shown by variation in porosity in z-direction (Fig. 11c)
952 that is correlated with anisotropic permeability tensor (Eq. 6). At a larger scale, a higher degree of permeability
953 anisotropy is usually associated with the presence of localized beds, foliation, and compaction bands that
954 constitute barriers to flow in the perpendicular direction (see Halisch et al., 2009; Clavaud et al., 2008 and
955 references therein).

956 Flow modelling in the specified REV of S1 shows anisotropy (Table 2) and an average permeability value
957 of 310 mD that is close to that derived from MIP (330 mD). However, the average permeability is lower than

Deleted: 20

Deleted: indicates

Deleted: detected

Deleted: at a small scale

Deleted: Clay-free and cement-free layers constitute the main avenues for flow in the parallel direction, shown for S1 by variation in porosity in z-direction (Fig. 11c) that is correlated with anisotropic permeability matrix (Eq. 11).

Deleted: Clay-free and cement-free layers constitute the main avenues for flow in the parallel direction (e.g., Figure 12).

Deleted: The semivariogram analysis of S1 reveals horizontal porosity bands with a thickness of ~1.6 mm (Figure 12c) that are composed of larger or smaller grains with larger or smaller pores between them, correspondingly.

972 the average experimental gas permeability (~543 mD); this difference should be related to the loss of porosity
973 due to limitations on the CT resolution, image processing and meshing (Table 3, see Sect. 5.2 for more details).

974 In contrast, flow modelling and upscaling to the macro scale indicate an isotropic S3 sample (Eq.7).
975 However, the modelled permeability (~4500 mD) is ten times higher than the MIP-derived permeability (~466
976 mD, Table 2). Gas permeability measurements indicate anisotropy, yielding permeabilities of ~4600 mD in
977 the x-y plane and ~220 mD in the z-direction (with an anisotropy ratio of ~20, defined here as κ/κ_z , e.g., Tiab
978 and Donaldson, 2004). For comparison, the values of this ratio obtained from experimental permeability
979 measurements were ~1.2 for Bentheim sandstone (Louis et al., 2005), ~1.7-2.5 for a sandstone within the
980 Cretaceous Virgelle Member, Alberta, Canada (Meyer and Krause, 2001), and ~8.5 for Berea sandstone (Sato
981 et al., 2019). However, in our laboratory measurements conducted parallel to the layering (in the x-y plane),
982 poorly cemented grains in S3 could dislocate from the weakly consolidated sample due to the application of a
983 pressure gradient. This could have resulted in a higher measured gas flux and thus a higher permeability
984 parallel to the layering, yielding a high anisotropy.

985 Alternatively, the disagreement between the laboratory-determined permeability perpendicular to the
986 layering, κ_z , and the isotropic permeability obtained from the flow modelling (Table 2, Eq.7) may also stem
987 from the small dimension of the modelled REV domain (cube edge length of ~0.875 mm), which may not
988 have included the additional textural features (e.g., Figure 5d) that constrain fluid flow on a larger scale of the
989 lab sample of S3 (2.5 cm in diameter and 5-7 cm in length).

990 However, the consistency of the REV size in S3 by the additional permeability simulations on
991 equivalently REV sized segmented sub-volumes and on the entire sample (Figures 15, 16), is confirmed by
992 yielding nearly isotropic permeability tensors that are also in a good agreement with previously simulated
993 permeability tensor in the REV (Eq.7). The average permeability derived from all REV-sized sub-volumes is
994 ~4381 mD, compared to the average permeability of ~4500 mD simulated over the entire S3 geometry. This,
995 again, is in a good accordance with the gas permeability of S3 measured parallel to the layering (~4600 mD,
996 Table 2). These additional simulation results (Figure 16), strengthen our conclusion that those may not have
997 included the textural features that constrain fluid flow on a larger scale of the sample S3, tested by the
998 laboratory experiments. Similarly, the differences with the permeability estimated by MIP seem to originate
999 from the same reason.

Deleted: no banding was detected in S3 by the semivariogram analysis (Figures 13-14). F

Deleted: Table 2

Deleted: some

Deleted: In this case, the permeability upscaled from the modelling in S3 is also exaggerated.

Deleted: (

Deleted:)

Deleted: (e.g., Figure 5d)

Deleted: Nevertheless,

Deleted: verified

Deleted: of S3

Deleted: S3

Deleted: have been conducted, to ensure

Deleted: 8

Deleted: 9

Deleted: consistency of the estimated REV size.

Deleted: These simulations have been performed by using the FlowDict module (Linden et al., 2015; 2018) of the GeoDict toolbox (Wiegmann, 2019) currently available at our disposal. Pre-processing as well as boundary conditions are identical to those used in COMSOL setup described in the Methods Sect. Sub-volumes locations, detailed permeability tensor simulation results as well as evaluated 3D image porosity data, can be found within the Appendix C. The ...

Deleted: results

Deleted: that

Deleted: conducted flow simulations

Deleted: Table 2

Deleted: upon

Deleted: conducted in the sub-samples and in the full sample S3

Deleted: 9

Deleted: (Appendix C)

Deleted: s

Deleted: in the gas permeametry

Deleted: ,

1036 For sample S2, REV and slice-by-slice porosity analysis indicated an REV size larger than the
1037 investigated sample size (Figure 13c, 14). For this reason, the analytical programme formulated in our study
1038 cannot entirely be applied to S2 due to the impossibility of determining a reliable REV and hence conducting
1039 pore-scale flow modelling. As a result, although sample S2 represents a common sandstone, it is very
1040 heterogeneous in nature, and a sample larger than at least 9 mm (which is a maximal length in z-direction of
1041 the tested domain (Figure 13c)) is required to capture its REV. The MIP-derived permeability is 4 mD; this
1042 low permeability is due to a clay-rich matrix that encloses substantial void space (Hurst and Nadeau, 1995;
1043 Neuzil, 2019). The gas permeability of the quartz wacke layer (S2, ~4.6 mD on average) is approximately two
1044 orders of magnitude lower than that of the quartz arenite layers (S1 and S3, Table 2). The permeability
1045 anisotropy ratio of S2 is ~2.8. The high inverse correlation between the porosity and clay matrix content
1046 enhanced in the z-direction (Figures 13c, d) suggests that the clay matrix pattern appears as horizontal layering,
1047 thus generating the observed anisotropy.

1048 Finally, non-marine sandstones of Lower Cretaceous age (as well as sandstones in general), feature a
1049 big complexity and variability in their characteristics, as immediately seen even from a comparison of our
1050 samples S1, S2, S3 from the same outcrop (Table 2). For instance, low porosity of Wealden quartz arenite
1051 sandstones from Weald Basin within Ashdown and Wadhurst Clay Fms. in southeast England, ranges between
1052 6.3 % and 13.2 %, while permeability between 0.4 mD and 11.9 mD (Akinlotan, 2016), suggested to be
1053 controlled mainly by grain sizes, grain shapes, and sorting that are directly linked to their depositional
1054 environment. Average porosities of 3.06 % and 0.19 % were evaluated in medium and fine grained
1055 tight gas sandstones, correspondingly, from Lower Cretaceous Dengloulou Fm. in the Songliao Basin,
1056 China (Zhang et al., 2019). Alternatively, a secondary porosity of 4 % to 22 % was generated by
1057 acidic fluids acting in the compactional regime, destructing a high primary porosity in sandstone of
1058 Lower Cretaceous Shurijeh Fm. in the eastern Kopet-Dagh Basin in NE Iran (Moussavi-Harami and
1059 Brenner, 1993). Significant average porosity and permeability of 20 % and 3700 mD, respectively,
1060 were quantified in the Masila Block, Upper Qishn Fm. of the Lower Cretaceous Age, Republic of
1061 Yemen (Harding et al., 2002). Multi-methodological approach suggested in this study is applicable
1062 to all those sandstones with broad ranges of their textural, topological and mineralogical
1063 characteristics and should lead to their accurate petrophysical characterization.

Deleted: both classic

Deleted: and semivariogram

Deleted: e

Deleted: 18

Deleted: , Figs. B1 c,d in Appendix A

Deleted: size

Deleted: [

Deleted:]

Deleted: , where porosity shows a trend with depth

Deleted: 5

Deleted: 16c

Deleted: The distinctions usually stem from the different depositional and diagenetic conditions.

Deleted:

Deleted: , while s

5.2. Upscaling permeability: accuracy of the extended computational workflow

The extended computational workflow (Figure 2) serves as the main tool in this study for upscaling permeability from the pore-scale velocity field. The accuracy of each step in the workflow affects the ultimate result.

Following the steps of the workflow, a micro-CT image resolution of 2.5 μm limits the reliability of the representation of the porous medium and defines the lower pore identification limit using this method. As an example of this limitation, the *SSA* (bulk specific surface area) calculated by MIP is larger than the *PSA* (pore specific surface area) calculated by micro-CT image analysis in all the samples (Table 2), although the pore volume is always smaller than the bulk volume. The *PSA* from micro-CT is limited by the image resolution and therefore does not consider relatively small pores with large surfaces. The *PSAs* of S1 and S3 are similar, but the *SSA* (from MIP) of S1 is 20 times larger than that of S3 because S1 has a larger surface area at small pores created mainly by Fe-ox cement (compare Figure 3c-f for S1 to Figure 5c for S3). In contrast to *SSA*, *PSA* in S2 is only twice as large as that of S1 due to the presence of clay and clay matrix with large surface areas.

Image processing and segmentation were applied in this study to recover the image geometry, which was blurred by noise or affected by the partial volume effect (see Sect. 3). Then, the loss of pore space due to the resolution limits was estimated in this study from the amount of mercury filling the pores with diameters equal to the resolution limit (Figure 7a). After segmentation, sample S1 had a segmented image porosity of 17.5 % and a CT predicted porosity of 23.5 % from MIP (Tables 2, 3). Therefore, the difference in porosities generated by the partial volume effect in the image processing scheme (e.g., Cnudde and Boone, 2013) is a significant component of error, especially for small structures, such as pores with a large surface area-to-volume ratio. In contrast, the image porosity of S3 after segmentation was 28.3 %, which is close to the porosity of 30.4 % estimated from MIP (Tables 2, 3). This is a result of the very small degree of cementation and the absence of Fe-ox flakes in the majority of the sample pores, leading to the small contribution of the partial volume

Deleted: S2 shows a

effect. In comparison, a fine-grained and well-sorted Lower Cretaceous Fm. sandstone from Heletz Field (e.g., Figure 1a) (Tatomir et al., 2016) comprising clay and calcite, had MIP and micro-CT porosities of 26.7 % and 20.9 %, respectively.

An additional source of inaccuracy is the use of a porosity-based REV for permeability approximations. Mostaghimi et al. (2012) showed that for CT images of sandpacks (homogenous samples), the porosity-based REV had an edge length of 0.5 mm, whereas the permeability-based REV was twice as large. Moreover, the porosity- and permeability- based REVs in images of crushed bead packs derived by Zhang et al. (2000) had edge lengths of 1.71 and 2.57 mm, respectively. According to Mostaghimi et al. (2012), larger REV values for permeability rely on contributions from the tortuosity and connectivity of pore spaces, whereas the larger REV values of Zhang et al. (2000) might be related to the heterogeneity of the sample.

This discrepancy indicates a larger REV for a rock property evaluated using physics-based simulations than for those estimated using morphology-based methods (Saxena et al., 2018 and references therein). Furthermore, implementing the classic REV determination methodology (e.g., Callow et al., 2020) using very small search sub-volumes is not in agreement with capturing a sufficient structural complexity (Saxena et al., 2018).

Flow simulations performed in sub-volumes and full sample of S3 (Figures 15, 16) support this conclusion. Small dimensions of the evaluated REV (~ 0.875 mm) of homogeneous S3 ensure efficient calculations. Both, porosity and permeability demonstrate a good agreement (Table 2, Figure 16), thus confirming a representativeness of the estimated REV and a continuity of these characteristics over the chosen sample. However, the differences in porosity between the sub-samples and the full sample are smaller than the corresponding differences in permeability (Figure 16), as anticipated from the porosity-based REV derivation discussed above.

An additional verification of the REV size for flow simulations in S3 follows the approach given by Saxena et al. (2018). They demonstrated that for homogeneous sandstones, the smallest pore throats can be accurately resolved at $N_I > 10$, where $N_I = D_D / \Delta x$ is a ratio of the pore throat size corresponding to mercury entry pressure, D_D , and of the voxel size, Δx . N_I controls the lower bound on permeability that can be reliably calculated using a digital rock image, to capture sufficient structural complexity of rock microstructure which affects flow, attributed to D_D visualized using Δx . For our sub-volumes of sample S3 imaged with $\Delta x = 2.5 \mu\text{m}$ resolution, and $D_D = 35 \mu\text{m}$ (Table 2), $N_I = 14 > 10$. In addition, there is a requirement for the minimal

135 REV size for representativeness for permeability calculation, $N_{REV} = L/D_{eff} \geq 5$ (Saxena et al., 2018), where
 136 L is a digital rock (i.e., domain) length, and D_{eff} is the effective grain diameter (e.g., Říha et al., 2018). For
 137 S3 sub-volumes with $L = 875 \mu\text{m}$ REV size and $D_{eff} = 58.6 \mu\text{m}$ (computed from laboratory grain size data
 138 which includes both sand and fines, Figure 6), this requirement is achieved as well: $N_{REV} = 15 > 5$, which
 139 also proves the reliability of the sub-volume permeability modelling with the presented approach. The
 140 calculations in sub-volume performed with Comsol (Eq. 7, Table 2) demonstrate the smallest deviation in
 141 mean permeability compared to that in the full sample (0.85 %). In comparison, other sub-volumes modelled
 142 with GeoDict (Figure 16) have larger mean permeability deviations from the full sample (ranging between 5
 143 % and 17 %), still demonstrating a very good agreement with those conducted on the full-scale S3 domain.

144 Further, according to Saxena et al. (2018), REV size supported by N_{REV} for flow simulations, should
 145 also be insensitive to the choice of boundary conditions, which effect on tensorial flow properties diminishes
 146 with an increasing sample size (e.g., Guibert et al., 2016; Gerke et al., 2019). No-slip boundary conditions
 147 applied in our study at four lateral faces of the modelling domains, correspond to those in the experimental
 148 permeability measurements and are also the most commonly used boundary conditions for the pore-scale flow
 149 simulations (Guibert et al., 2016 and references therein). However, they were recently shown to suppress the
 150 transversal flow through the simulation domain to some extent, resulting in deviation in alignment of the
 151 permeability tensor and in underestimation of its magnitude (Gerke et al., 2019) even at REV dimensions.
 152 Thus, the difference in the mean permeability derived from all REV-sized sub-volumes (~ 4381 mD) and that
 153 simulated over the entire S3 geometry (~ 4500 mD) (Figure 16) can also be attributed to this effect. For the
 154 future studies we suggest that determining REV size for the flow simulation from porosity is justified, by
 155 acknowledging the typical ratio of two between those for permeability and porosity.

156 To upscale to permeability reliably, the REV domain should be sufficiently large such that it is bounded
 157 from below by the scale of the textural bedding, but should not be larger than necessary to optimize the
 158 computational efficiency (while remaining within the same scale of heterogeneity, i.e., at the macro scale). As
 159 a result, a REV with an edge length of ~2950 μm was chosen in the current study in sample S1, based on slice-
 160 by-slice porosity profiles that reveal mm-scale layering in the z-direction (Figure 11c), rather than on the
 161 classic isotropic REV approach. For comparison, in other studies, the edge lengths of REV in sandstones were
 162 0.68 mm (Ovaysi and Piri, 2010), 0.8 mm (Mostaghimi et al., 2012), and 1.2 mm (Okabe and Oseto, 2006;
 163 Tatomir et al., 2016) derived by the classic approach. In contrast to the classic REV estimation, where porosity

Deleted: ¶

***¶

Further, textural bedding at ~1.6 mm scale dominates the porosity anisotropy in S1 (Figure 12c, evaluated by the semivariogram), and by ~3.5 mm average thickness of two adjacent more and less porous beddings together.

Deleted: (i.e., an edge length > 3.5 mm)

Deleted: (~1.5 times larger than the scale of textural bedding)

Deleted: 2013

Deleted: The larger REV size in the current study found was implied from slice-by-slice porosity by the semivariogram (rather than by the classic isotropic approach) was due to the textural features (mm scale layering) revealed in the z-direction, which were originated from depositional processes.

Deleted: .

Deleted: While

Deleted: al

Deleted: porosity analyses

Deleted: the data without

1183 analysis does not consider directionality, 1D profiles from slice-by-slice porosity provides additional
1184 information on anisotropy and inhomogeneity of the sample which have implications on the ultimate
1185 determination of the REV. In the future studies, the 1D profiles can be used to calculate spatial correlation
1186 length (e.g., using variogram analyses) of geological structures, that include layering, as in S1 in the current
1187 study.

Deleted: ing

Deleted: the heterogeneity

Deleted: T

Deleted: which may be relevant for the geological REV

Deleted: (e.g.

Deleted:)

1188 Another source of inaccuracy is the geometry used for the flow model. The geometry considered in this
1189 study included only the pore network connecting six faces of the REV cube. Other pore spaces in the REV
1190 disconnected from the main network were deleted (because all paths smaller than the resolution were
1191 prescribed as grain pixels due to the partial volume effect), thus resulting in the smaller effective size of the
1192 simulation domain. The image porosity of sample S1 was 17.5 %, whereas its connected porosity was
1193 estimated as 15.6 % (Table 3), while those of sample S3 were 28.3 % and 27.9 %, respectively.

1194 Furthermore, the mesh was generated by taking a trade-off between the size of the mesh elements (4
1195 elements in the smallest pore throat) and computational limits into account, while coarsening the mesh
1196 elements towards the pore centre. The connectivity between pores with very fine pore throats that could not
1197 be replaced by mesh elements could be lost, resulting in the loss of those pores in the calculations. In sample
1198 S1, the porosity used in the simulation was approximately 50 % smaller than the porosity estimated by gas
1199 porosimetry (Tables 2, 3). In contrast, the porosity used in the simulations in S3 was mostly preserved,
1200 comprising ~84 % of that estimated in the laboratory.

1201 For comparison, in the fine-grained sample of the Lower Cretaceous sandstone from Heletz Field in
1202 Israel (Figure 1a), which has grain size characteristics similar to those of S1 but with higher clay and additional
1203 calcite contents (Tatomir et al., 2016), the permeability upscaled from micro-CT flow modelling (conducted
1204 by the same simulation method as that in the current study) exceeded the gas permeability by a factor of ~7.
1205 This could be related to the reduction in the specific surface area by image processing and meshing
1206 (Mostaghimi et al., 2012) conducted for the flow modelling.

Deleted: 6

Deleted: 10

Deleted: (Table 2)

Deleted: 3

1207 Finally, the upscaling process from the flow modelling successfully predicted the permeability
1208 anisotropy ratio of ~2.3 in S1, as discussed above. For comparison, the permeability anisotropy ratio evaluated
1209 using micro-CT flow monitoring in clay-free sandstones (Clavaud et al., 2008) had a mean value of ~2.5
1210 (ranging from ~1.7 to ~5.2), related to the presence of less permeable silty layers. This is consistent with the

Deleted: This could be related either to the small REV for the flow model or to the reduction in the specific surface area by image processing and meshing (Mostaghimi et al., 2013) for the flow modelling.

ratio estimated at the pore scale in Rothbach sandstone (~5) (Louis et al., 2005), attributed to lamination due to differences both in the characteristics of the solid phase (grain size and packing) and in the content of the Fe-ox.

6. Conclusions

This paper presents a detailed description and evaluation of a multi-methodological petrophysical approach for the comprehensive multiscale characterization of reservoir sandstones. The validation was performed on samples from three different consecutive layers of Lower Cretaceous sandstone in northern Israel. The following conclusions can be drawn:

1. The suggested methodology enables the identification of links between Darcy-scale permeability and an extensive set of geometrical, textural and topological rock descriptors. Specifically, micro-scale geometrical rock descriptors (grain and pore size distributions, pore throat size, characteristic length, pore throat length of maximal conductance, specific surface area, and connectivity index) and macro-scale petrophysical properties (porosity and tortuosity), along with anisotropy and inhomogeneity, are used to predict the permeability of the studied layers.
2. Laboratory porosity and permeability measurements conducted on centimetre-scale samples show less variability for the quartz arenite (top and bottom) layers and more variability for the quartz wacke (intermediate) layer. The magnitudes of this variability in the samples are correlated with the dimensions of their representative volumes and anisotropy, both of which are evaluated within the micro-CT-imaged 3D pore geometry. This variability is associated with clay and cementation patterns in the layers.
3. Two different porosity variation patterns are revealed in the top quartz arenite layer: fluctuations at ~100 µm half wavelength in all direction, associated with an average pore cross-section, and those at ~3.5 mm wavelength in the vertical direction only, associated with the occurrence of high- and low-porosity horizontal bands occluded by Fe-ox cementation. The latter millimetre-scale variability is found to control the macroscopic rock permeability measured in the

Deleted: In this study we used the semivariogram range of spatial correlation of porosity as a parameter to determine the REV from CT data (in addition to the classic method suggested by Bear, 2013). The spatial correlation of porosity relates to a distance that fluid travels without being constrained by grains, and therefore to permeability. Calibrating the range of correlation of porosity by modelling the semivariogram for different sub-volume sizes sheds light on the specimen heterogeneity at the different scales. This approach could be applied for a series of CT datasets, to determine the REV from the range of correlations and to compare to the REV of permeability. Quantifying the spatial variability of structures which occur at different sub-volume sizes, may link to generation of preferential flow paths and to determination of effective porosity (associated with mobile water fraction) that is available for transport. ¶

Deleted: , which are quantified at the pore scale by deterministic and statistical methods

Deleted: quantified

Deleted: and is quantified in this study with image and semivariogram analyses

Deleted: correlation lengths of

Deleted: by statistical semivariogram analysis

Deleted: are due to variability in grain and pore sizes

Deleted: 1.6

Deleted: are due to

laboratory. Bands of lower porosity could be generated by Fe-ox cementation in regions with higher surface areas adjacent to preferential fluid flow paths.

4. More heterogeneous pore structures were revealed in the quartz wacke sandstone of the intermediate layer. This heterogeneity resulted mainly from the presence of patchy clay deposition structure.

5. Quartz arenite sandstone of the bottom layer shows stationarity in the investigated domain and lower anisotropy characteristics than that of the top layer, due to less horizontal cement bands.

6. The macroscopic permeability upscaled from the pore-scale velocity field simulated by flow modelling in the micro-CT-scanned geometry of millimetre-scale sample shows agreement with laboratory petrophysical estimates obtained for centimetre-scale samples for the quartz arenite layers. Comparison of permeability tensors evaluated in multiple REV sub-volumes and in the full segmented sample of the bottom layer, shows a particular agreement attributed to the homogeneity of this sample.

7. The multi-methodological petrophysical approach detailed and evaluated in this study allows the accurate petrophysical characterization of reservoir sandstones with broad ranges of textural and topological features.

Acknowledgements

This project was supported by fellowships from the Ministry of Energy, Israel, and the University of Haifa. The authors are grateful to Igor Bogdanov from the University of Pau for his continuing scientific support. Special thanks to Rudy Swennen and his group from KU Leuven for their contributions to the MIP, thin section preparation, microscopy and micro-CT image processing; to Veerle Cnudde and her group from Ghent University for teaching us the image processing techniques; to Kirill Gerke and Timofey Sizonenko from the Russian Academy of Sciences for providing their image processing code; to Uzi Saltzman from Engineering Geology and Rock Mechanics Company, Israel, for sending his detailed historic geological description of the study area; and to Or Bialik, Nimer Taha and Ovie Emmanuel Eruteya from the University of Haifa, Israel, for their assistance in the laboratory work. We thank the editor and two anonymous reviewers for their significant contribution in enhancing this paper.

Deleted: from a combination of several spatial structures, each one with an internal irregularity: the pore size at the scale of ~50 μm , the distance between the pores at the scale of ~350 μm , and the larger-scale more porous “lense” structures originated at

Deleted: at the ~1-2 mm distance

Deleted: Modelling of the experimental semivariograms indicates a scale of ~0.1 mm in all directions, associated with the average size of pore cross-section.

Deleted: The anisotropy in both estimates correlates with the presence of millimetre-scale bedding.

Deleted: also recognized by the semivariogram analysis.

Deleted: is particularly applicable for the detection of anisotropy at various rock scales and for the identification of its origin. Moreover, this method

1318 **Competing interests**

1319 The authors declare that they have no conflicts of interest.

1320

1321 **Author contributions**

1322 PH and RK designed the study. PH developed codes for pore-scale modelling with contributions by RK and

1323 MH. BS advised the microscopy and led the geological interpretations. MH scanned the samples, NW led the

1324 laboratory measurements. All co-authors participated in the analysis of the results. PH wrote the text with

1325 contributions from all co-authors. All co-authors contributed to the discussion and revisions and approved the

1326 paper.

1327

1328 **Supplementary Material & Data Availability**

1329 3-D μ -CT datasets are freely available at the open access data repository “PANGAEA” under the given doi:

1330 <https://doi.pangaea.de/10.1594/PANGAEA.907552>.

1331

Deleted: and contributed to the statistical analysis conducted by PH...

1334 References

- 1335 Abed, A. M.: Depositional environments of the early cretaceous Kurnub (Hatira) sandstones, North Jordan,
1336 Sedimentary Geology, 31(3-4), 267-279, **1982**.
- 1337 Akinlotan, O.: Porosity and permeability of the English (Lower Cretaceous) sandstones, Proceedings of the
1338 Geologists' Association, 127, 681-690, **2016**.
- 1339 Akinlotan, O.: Mineralogy and palaeoenvironments: the Weald Basin (Early Cretaceous), Southeast England,
1340 The Depositional Record, 3(2), 187-200, **2017**.
- 1341 Akinlotan, O.: Multi-proxy approach to palaeoenvironmental modelling: the English Lower Cretaceous Weald
1342 Basin, Geol. J. 53, 316–335, **2018**.
- 1343 Ambegaokar, V., Halperin, B. I., & Langer, J. S. (1971). Hopping conductivity in disordered systems. *Physical*
1344 *review B*, 4(8), 2612.
- 1345 American Petroleum Institute, API : Recommended Practices for Core Analysis, RP 40, second edition, **1998**.
- 1346 Amireh, B. S.: Sedimentology and palaeogeography of the regressive-transgressive Kurnub Group (Early
1347 Cretaceous) of Jordan, Sedimentary Geology, 112(1-2), 69-88., **1997**.
- 1348 Andrä, H., Combaret, N., Dvorkin, J., Glatt, E., Han, J., Kabel, M., Keehm. Y., Krzikalla, F., Lee, M.,
1349 Madonna, C., Marsh, M., Mukerji, T., Saenger, E., Sain, R., Saxena, N., Ricker, S., Wiegmann, A., and
1350 Zhan, X.: Digital rock physics benchmarks-Part I: Imaging and segmentation, Computers & Geosciences,
1351 50, 25-32, **2013a**.
- 1352 Andrä, H., Combaret, N., Dvorkin, J., Glatt, E., Han, J., Kabel, M., Keehm. Y., Krzikalla, F., Lee, M.,
1353 Madonna, C., Marsh, M., Mukerji, T., Saenger, E., Sain, R., Saxena, N., Ricker, S., Wiegmann, A., and
1354 Zhan, X.: Digital rock physics benchmarks-Part II: Computing effective properties, Computers &
1355 Geosciences, 50, 33-43, **2013b**.
- 1356 Arns, J.Y., Sheppard, A.P., Arns, C.H., Knackstedt, M.A., Yelkhovsky, A., and Pinczewski, W.V.: Pore-level
1357 validation of representative pore networks obtained from micro-CT images. In: Proceedings of the annual
1358 symposium of the society of core analysis, SCA2007-A26, Calgary, Canada, **2007**.
- 1359 Asakawa, S., Watanabe, T., Lyu, H., Funakawa, S. and Toyohara, H.: Mineralogical composition of tidal flat
1360 sediments in Japan, Soil Science and Plant Nutrition, 1-9, **2020**.
- 1361 Avigad, D., Kolodner, K., McWilliams, M., Persing, H., and Weissbrod, T.: Origin of northern Gondwana
1362 Cambrian sandstone revealed by detrital zircon SHRIMP dating, Geology, 31(3), 227-230, **2003**.
- 1363 Avigad, D., Sandler, A., Kolodner, K., Stern, R. J., McWilliams, M., Miller, N., and Beyth, M.: Mass-
1364 production of Cambro-Ordovician quartz-rich sandstone as a consequence of chemical weathering of Pan-
1365 African terranes: Environmental implications, Earth and Planetary Science Letters, 240(3-4), 818-826,
1366 **2005**.
- 1367 Bear, J.: Dynamics of fluids in porous media. Courier Corporation, **2013**.
- 1368 Blunt, M. J., Bijeljic, B., Dong, H., Gharbi, O., Iglauer, S., Mostaghimi, P., Paluszny, A., and Pentland, C.:
1369 Pore-scale imaging and modelling, Advances in Water Resources, 51, 197-216, **2013**.
- 1370 Boek, E. S., and Venturoli, M.: Lattice-Boltzmann studies of fluid flow in porous media with realistic rock
1371 geometries, Computers & Mathematics with Applications, 59(7), 2305-2314, **2010**.

1372 Bogdanov, I. I., Guerton, F., Kpahou, J., and Kamp, A. M.: Direct pore-scale modeling of two-phase flow
1373 through natural media, in: Proceedings of the 2011 COMSOL Conference in Stuttgart, **2011**.

1374 Bogdanov, I. I., Kpahou, J., and Guerton, F.: Pore-scale single and two-phase transport in real porous medium,
1375 in: Proceedings of ECMOR XIII-13th European Conference on the Mathematics of Oil Recovery,
1376 September, **2012**.

1377 Boudreau, B. P.: The diffusive tortuosity of fine-grained unlithified sediments, *Geochimica et Cosmochimica*
1378 *Acta*, 60(16), 3139-3142, **1996**.

1379 Brabant, L., Vlassenbroeck, J., De Witte, Y., Cnudde, V., Boone, M. N., Dewanckele, J., and Van Hoorebeke,
1380 L.: Three-dimensional analysis of high-resolution X-ray computed tomography data with Morpho+,
1381 *Microscopy and Microanalysis*, 17(2), 252-263, **2011**.

1382 Brunke, O., Brockdorf, K., Drews, S., Müller, B., Donath, T., Herzen, J., and Beckmann, F.: Comparison
1383 between X-ray tube based and synchrotron radiation based μ CT, in: *Developments in X-ray Tomography*
1384 VI, edited by: Stock, S. R., San Diego: SPIE, 7078, **2008**.

1385 [Callow, B., Falcon-Suarez, I., Marin-Moreno, H., Bull, J. M., and Ahmed, S. Optimal X-ray micro-CT image](#)
1386 [based methods for porosity and permeability quantification in heterogeneous sandstones](#), *Geophysical*
1387 [Journal International](#), 223(2), 1210-1229, **2020**.

1388 Calvo, R., The diagenetic history of Heletz Formation and the timing of hydrocarbons accumulation in Heletz-
1389 Kokhav oil field. M.Sc. thesis, The Hebrew University of Jerusalem, 72 p. (in Hebrew, with English
1390 abstract), **1992**.

1391 Calvo, R., Ayalon, A., Bein, A., and Sass, E.: Chemical and isotopic composition of diagenetic carbonate
1392 cements and its relation to hydrocarbon accumulation in the Heletz-Kokhav oil field (Israel), *Journal of*
1393 *Geochemical Exploration*, 108(1), 88-98, **2011**.

1394 Carman, P. C.: Fluid flow through granular beds, *Trans. Inst. Chem. Eng.*, 15, 150-166, **1937**.

1395 Cerepi, A., Durand, C., and Brosse, E.: Pore microgeometry analysis in low-resistivity sandstone reservoirs,
1396 *Journal of Petroleum Science and Engineering*, 35(3-4), 205-232, **2002**.

1397 Clavaud, J. B., Mainault, A., Zamora, M., Rasolofosaon, P., and Schlitter, C.: Permeability anisotropy and its
1398 relations with porous medium structure, *Journal of Geophysical Research: Solid Earth*, 113(B1), **2008**.

1399 Cnudde, V., and Boone, M. N.: High-resolution X-ray computed tomography in geosciences: A review of the
1400 current technology and applications, *Earth-Science Reviews*, 123, 1-17, **2013**.

1401 Cohen, A., and Boehm, S.: Lithofacies and environments of deposition of the Lower Cretaceous Helez &
1402 Telamim Formations, Geological Survey of Israel Report No. 5, **1983**.

1403 Cohen, Z.: The geology of the Lower Cretaceous in Southern Coastal Plain, Ph.D. thesis, The Hebrew
1404 University of Jerusalem, 98 pp. (in Hebrew, with English abstract), **1971**.

1405 Cressie, N.: Fitting variogram models by weighted least squares. *Journal of the international Association for*
1406 *mathematical Geology*, 17(5), 563-586, **1985**.

1407 Du, S., Pang, S., and Shi, Y.: Quantitative characterization on the microscopic pore heterogeneity of tight oil
1408 sandstone reservoir by considering both the resolution and representativeness, *J. Pet. Sci. Eng.*, 169, 388–
1409 392, **2018**.

1410 Dullien, F. A.: Porous media: fluid transport and pore structure, Academic press, **2012**.

1411 Harter, T.: Finite-size scaling analysis of percolation in three-dimensional correlated binary Markov chain
 1412 random fields, *Physical Review E*, 72(2), 026120, **2005**.

1413 Farrel, N.J.C., Healy, D., and Taylor, C.W.: Anisotropy of permeability in faulted porous sandstones. *Journal*
 1414 *of Structural Geology* 63, 50-67, **2014**.

1415 Ferreira, N. N., Ferreira, E. P., Ramos, R. R., and Carvalho, I. S.: Palynological and sedimentary analysis of
 1416 the Igarapé Ipiranga and Querru 1 outcrops of the Itapecuru Formation (Lower Cretaceous, Parnaíba
 1417 Basin), Brazil, *Journal of South American Earth Sciences*, 66, 15-31, **2016**.

1418 Folk, R. L., and Ward, W. C.: Brazos River bar [Texas]; a study in the significance of grain size parameters,
 1419 *Journal of Sedimentary Research*, 27(1), 3-26, **1957**.

1420 Gardosh, M. A., and Tannenbaum, E.: The petroleum systems of Israel, in: *Petroleum systems of the Tethyan*
 1421 *region: AAPG Memoir*, edited by: Marlow, L., Kendall, C., and Yose, L., 106, 179-216, **2014**.

1422 Garfunkel, Z.: The pre-quaternary geology in Israel, in: *The zoogeography of Israel*, edited by: Tchernov, E.,
 1423 and Yom-Tov, Y., Dr W. Junk Publishers, Dordrecht, Netherlands, 7-34, **1988**.

1424 Garfunkel, Z.: History and paleogeography during the Pan-African orogen to stable platform transition:
 1425 reappraisal of the evidence from the Elat area and the northern Arabian-Nubian Shield, *Israel Journal of*
 1426 *Earth Sciences*, 48, 135-157, **1999**.

1427 [Gerke, K. M., Karsanina, M. V., and Katsman, R.: Calculation of tensorial flow properties on pore level:](#)
 1428 [Exploring the influence of boundary conditions on the permeability of three-dimensional stochastic](#)
 1429 [reconstructions, *Physical Review E*, 100, 053312, 2019.](#)

1430 Giesche, H.: Mercury porosimetry: a general (practical) overview. *Particle & particle systems characterization*,
 1431 23(1), 9-19, **2006**.

1432 Grader, P., and Reiss, Z.: On the Lower Cretaceous of the Heletz area, *Geological Survey of Israel, Bull No.*
 1433 16, 14 pp., **1958**.

1434 Grader, P.: The geology of the Heletz oil field, Ph.D. thesis, The Hebrew University of Jerusalem, 81 pp. (in
 1435 Hebrew, with English abstract), **1959**.

1436 Gringarten, E., and Deutsch, C.V.: Teacher's aide semivariogram interpretation and modeling. *Mathematical*
 1437 *Geology*, 33(4), 507-534, **2001**.

1438 Guibert, R., Horgue, P., Debenest, G., and Quintard, M.: A comparison of various methods for the numerical
 1439 evaluation of porous media permeability tensors from pore-scale geometry, *Mathematical Geosciences*,
 1440 48(3), 329-347, **2016**.

1441 Haldorsen, H. H., and Lake, L. W.: A new approach to shale management in field-scale models, *Society of*
 1442 *Petroleum Engineers Journal*, 24(04), 447-457, **1984**.

1443 Halisch, M.: Application and assessment of the lattice boltzmann method for fluid flow modeling in porous
 1444 rocks, PhD thesis, Technical University of Berlin, 182 pp., **2013a**.

1445 Halisch, M.: The REV Challenge – estimating representative elementary volumes and porous rock
 1446 inhomogeneity from high resolution micro-CT data sets, *Society of Core Analysts (SCA) Proceedings*,
 1447 SCA2013-069, **2013b**.

1448 Halisch, M., Weller, A., Debschütz, W., Sattler, C. D., and El-Sayed, A. M.: A complex core-log case study
 1449 of an anisotropic sandstone, originating from Bahariya Formation, Abu Gharadig Basin, Egypt,
 1450 *Petrophysics*, 50(06), **2009**.

1451 Haoguang, W. E. I., Kun, M. A., Xiang'an, Y. U. E., and Xinxin, W. A. N. G.: The Relationship of Ultra-Low
 1452 Permeability Sandstone Aspect Ratio With Porosity, Permeability, *Advances in Petroleum Exploration*
 1453 and Development, 7(1), 7-12, **2014**.

1454 Harding, T. G., Norris, B., and Smith, K.H.: Horizontal Water Disposal Well Performance in a High Porosity
 1455 and Permeability Reservoir Conference: SPE International Thermal Operations and Heavy Oil
 1456 Symposium and International Horizontal Well Technology Conference.
 1457 SPE-18153-MS, <https://doi.org/10.2118/79007-MS>, **2002**.

1458 Hurst, A., and Nadeau, P. H.: Clay microporosity in reservoir sandstones: an application of quantitative
 1459 electron microscopy in petrophysical evaluation, *AAPG bulletin*, 79(4), 563-573, **1995**.

1460 Iassonov, P., Gebrenegus, T., and Tuller, M.: Segmentation of X-ray computed tomography images of porous
 1461 materials: A crucial step for characterization and quantitative analysis of pore structures, *Water Resources*
 1462 *Research*, 45(9), **2009**.

1463 Jackson, M. D., Muggeridge, A. H., Yoshida, S., and Johnson, H. D.: Upscaling permeability measurements
 1464 within complex heterolithic tidal sandstones, *Mathematical Geology*, 35(5), 499-520, **2003**.

1465 Kalaydjian, F.: Origin and quantification of coupling between relative permeabilities for two-phase flows in
 1466 porous media, *Transport in porous media*, 5(3), 215-229, **1990**.

1467 Kass, M., Witkin, A., and Terzopoulos, D.: Snakes: Active contour models, *International Journal of Computer*
 1468 *Vision*, 1(4), 321-331, **1988**.

1469 Katz, A. J., and Thompson, A. H.: Prediction of rock electrical conductivity from mercury injection
 1470 measurements, *Journal of Geophysical Research: Solid Earth*, 92(B1), 599-607, **1987**.

1471 Kerckhofs, G., Schrooten, J., Van Cleynenbreugel, T., Lomov, S. V., and Wevers, M.: Validation of x-ray
 1472 micro-focus computed tomography as an imaging tool for porous structures, *Review of Scientific*
 1473 *Instruments*, 79(1), 013711, **2008**.

1474 Khan, F., Enzmann, F., and Kersten, M.: Multi-phase classification by a least-squares support vector machine
 1475 approach in tomography images of geological samples, *Solid Earth*, 7(2), 481-492, **2016**.

1476 Knackstedt, M., Jaime, P., Butcher, A.R., Botha, P.W.S.K., Middleton, J., and Sok, R.: Integrating reservoir
 1477 characterization: 3D dynamic, petrophysical and geological description of reservoir facies. In:
 1478 Proceedings of the SPE Asia Pacific oil and gas conference and exhibition, 18–20 October, 2010,
 1479 Brisbane, Queensland, Australia, SPE 133981, **2010**.

1480 Kolodner, K., Avigad, D., Ireland, T. R., and Garfunkel, Z.: Origin of Lower Cretaceous ('Nubian') sandstones
 1481 of North-east Africa and Arabia from detrital zircon U-Pb SHRIMP dating, *Sedimentology*, 56(7), 2010-
 1482 2023, **2009**.

1483 Kozeny, J.: Über kapillare leitung der wasser in boden, *Royal Academy of Science, Vienna, Proceedings Class*
 1484 *I*, 136, 271-306, **1927**.

1485 Krinsley, D. H., Pye, K., Boggs Jr, S., and Tovey, N. K.: Backscattered scanning electron microscopy and
 1486 image analysis of sediments and sedimentary rocks. Cambridge University Press, **2005**.

1487 Lenormand, R.: Sca2003-52: Interpretation of mercury injection curves to derive pore size distribution, in:
1488 Proceedings of 2003 International Symposium of SCA., **2003**.

1489 Legland, D., Arganda-Carreras, I., Andrey, P.: MorphoLibJ: integrated library and plugins for mathematical morphology
1490 with ImageJ. *Bioinformatics*, 32(22), 3532-3534, **2016**.

1491 Li, Y., He, D., Chen, L., Mei, Q., Li, C., and Zhang, L.: Cretaceous sedimentary basins in Sichuan, SW China:
1492 Restoration of tectonic and depositional environments, *Cretaceous Research*, 57, 50-65, **2016**.

1493 Linden, S., Wiegmann, A., and Hagen, H.: The LIR space partitioning system applied to the Stokes equations,
1494 *Graph. Models* 82, 58–66 (2015).

1495 Linden S., Cheng L., Wiegmann A.: Specialized methods for direct numerical simulations in porous media,
1496 Math2Market GmbH, technical report, <https://doi.org/10.30423/report.m2m-2018-01>. **2018**.

1497 Liu, X., Wang, J., Ge, L., Hu, F., Li, C., Li, X., Yu, J., Xu, H., Lu, S., and Xue, Q.: Porescale characterization
1498 of tight sandstone in Yanchang Formation Ordos Basin China using micro-CT and SEM imaging from
1499 nm- to cm-scale, *Fuel*, 209, 254–264, **2017**.

1500 Lewis, J.J.M.: Outcrop-derived quantitative models of permeability heterogeneity for genetically different
1501 sand bodies. In: SPE Annual Technical Conference and Exhibition, 2-5 October 1988, Houston, Texas,
1502 **1988**.

1503 Louis, L., David, C., Metz, V., Robion, P., Menendez, B., and Kissel, C.: Microstructural control on the
1504 anisotropy of elastic and transport properties in undeformed sandstones. *International journal of rock*
1505 *mechanics and mining sciences*, 42(7-8), 911-923, **2005**.

1506 Massaad, M.: Origin and environment of deposition of Lebanon basal sandstones, *Eclogae Geologicae*
1507 *Helveticae*, 69(8), **1976**.

1508 Mckay, G., Use of Adsorbents for the Removal of Pollutants from Wastewater. CRC press, **1995**.

1509 MacKenzie, W. S., Adams, A. E., & Brodie, K. H. *Rocks and Minerals in Thin Section: A Colour Atlas*. CRC Press.,
1510 **2017**.

1511 Meyer, R., and Krause, F. F.: A comparison of plug-derived and probe-derived permeability in cross-bedded
1512 sandstones of the Virgelle Member, Alberta, Canada: The influence of flow directions on probe
1513 permeametry, *AAPG bulletin*, 85(3), 477-489, **2001**.

1514 Meyer, R.: Anisotropy of Sandstone Permeability. CREWES Research Report, Vol. 14, 2002.

1515 Mostaghimi, P., Blunt, M. J., and Bijeljic, B.: Computations of absolute permeability on micro-CT images,
1516 *Mathematical Geosciences*, 45(1), 103-125, **2012**.

1517 Moussavi-Harami, R., and Brenner, R. L.: Diagenesis of non-marine petroleum reservoirs: the Neocomian
1518 (Lower Cretaceous) Shurijeh Formation, Kopet-Dagh basin, NE Iran. *Journal of Petroleum Geology*,
1519 16(1), 55-72, **1993**.

1520 Munawar, M.J., Lin, C., Cnudde, V., Bultreys, T., Dong, C., Zhang, X., De Boever, W., Zahid, M.A., and Wu,
1521 Y.: Petrographic characterization to build an accurate rock model using micro-CT: case study on low-
1522 permeable to tight turbidite sandstone from Eocene Shahejie Formation, *Micron* 109, 22–33, **2018**.

1523 Narsilio, G. A., Buzzi, O., Fityus, S., Yun, T. S., and Smith, D. W.: Upscaling of Navier-Stokes equations in
1524 porous media: Theoretical, numerical and experimental approach, *Computers and Geotechnics*, 36(7),
1525 1200-1206, **2009**.

Deleted: 2013

1527 Nelson, P. H.: Pore-throat sizes in sandstones, tight sandstones, and shales, AAPG bulletin, 93(3), 329-340,
1528 **2009**.

1529 Neuzil, C. E.: Permeability of Clays and Shales, Annual Review of Earth and Planetary Sciences, 47, 247-273,
1530 **2019**.

1531 Nordahl, K., and Ringrose, P. S.: Identifying the representative elementary volume for permeability in
1532 heterolithic deposits using numerical rock models, Mathematical Geosciences, 40(7), 753, **2008**.

1533 Nordahl, K., Ringrose, P. S., and Wen, R.: Petrophysical characterisation of a heterolithic tidal reservoir
1534 interval using a process-based modelling tool, Petroleum Geoscience, 11, 17-28, **2005**.

1535 Norris, R. J., and J. J. M. Lewis. The geological modeling of effective permeability in complex heterolithic
1536 facies, in SPE Annual Technical Conference and Exhibition, Society of Petroleum Engineers, **1991**.

1537 Okabe, H., and Oseto, K.: Pore-scale heterogeneity assessed by the lattice-Boltzmann method, Society of Core
1538 Analysts (SCA2006-44), 12-16, **2006**.

1539 Ovaysi, S., and Piri, M.: Direct pore-level modeling of incompressible fluid flow in porous media, Journal of
1540 Computational Physics, 229(19), 7456-7476, **2010**.

1541 Pettijohn, F. J., Potter, P. E., and Siever, R.: Sand and Sandstone. Springer Verlag, 2nd ed., New York, **1987**.

1542 Ploner, A.: The use of the variogram cloud in geostatistical modelling, *Environmetrics: The official journal of*
1543 *the International Environmetrics Society*, 10(4), 413-437, **1999**.

1544 Pyrcz, M. J., and Deutsch, C. V.: The whole story on the hole effect. Geostatistical Association of Australasia,
1545 Newsletter, 18, 3-5, **2003**.

1546 Renard, P., Genty, A., and Stauffer, F.: Laboratory determination of the full permeability tensor, Journal of
1547 Geophysical Research: Solid Earth, 106(B11), 26443-26452, **2001**.

1548 Reynolds, A. D.: Paralic reservoirs. Geological Society, London, Special Publications, 444(1), 7-34, **2017**.

1549 Řiha, J., Petrula, L., Hala, M., and Alhasan, Z. Assessment of empirical formulae for determining the hydraulic
1550 conductivity of glass beads, Journal of Hydrology and Hydromechanics, 66(3), 337-347, 2018.

1551 Ringrose, P., and Bentley, M.: Reservoir Model Design: A Practitioner's Guide, Springer, 249 p. New York,
1552 **2015**.

1553 Rootare, H. M., and Prenzlów, C. F.: Surface areas from mercury porosimeter measurements, The Journal of
1554 physical chemistry, 71(8), 2733-2736, **1967**.

1555 RP40, A. P. I. (1960). API recommended practice for core-analysis procedure. *Edition, API, New York*, 12-13.

1556 Rustad, A. B., Theting, T. G., and Held, R. J.: Pore space estimation, upscaling and uncertainty modelling for
1557 multiphase properties. In SPE Symposium on Improved Oil Recovery, Society of Petroleum Engineers,
1558 **2008**.

1559 Saltzman, U.: Survey of the southeastern flanks of Mount Hermon, Tahal report (in Hebrew), **1968**.

1560 Sato, M., Panaghi, K., Takada, N., and Takeda, M.: Effect of Bedding Planes on the Permeability and
1561 Diffusivity Anisotropies of Berea Sandstone, Transport in Porous Media, 127(3), 587-603, **2019**.

1562 Saxena, N., Hows, A., Hofmann, R., Alpak, F. O., Freeman, J., Hunter, S., and Appel, M. Imaging and
1563 computational considerations for image computed permeability: operating envelope of digital rock
1564 physics, Advances in Water Resources, 116, 127-144, 2018.

1565 Schindelin, J., Arganda-Carreras, I., Frise, E., Kaynig, V., Longair, M., Pietzsch, T., Preibisch, S., Rueden,
 1566 C., Saalfeld, S., Schmid, B., Tinevez, J., White, D., Hartenstein, V., Eliceiri, K., Tomancak, P., and
 1567 Cardona, A.: Fiji: an open-source platform for biological-image analysis, *Nature methods*, 9(7), 676, **2012**.
 1568 Schlüter, S., Sheppard, A., Brown, K., and Wildenschild, D.: Image processing of multiphase images obtained
 1569 via X-ray microtomography: a review, *Water Resources Research*, 50(4), 3615-3639, **2014**.
 1570 Schmitt, M., Halisch, M., Müller, C., and Fernandes, C. P.: Classification and quantification of pore shapes in
 1571 sandstone reservoir rocks with 3-D X-ray micro-computed tomography, *Solid Earth*, 7(1), 285-300, **2016**.
 1572 Scholz, C., Wirner, F., Götz, J., Rüde, U., Schröder-Turk, G. E., Mecke, K., and Bechinger, C.: Permeability
 1573 of porous materials determined from the Euler characteristic, *Physical review letters*, 109(26), 264504,
 1574 **2012**.
 1575 Sethian, J. A.: A fast marching level set method for monotonically advancing fronts, *Proceedings of the*
 1576 *National Academy of Sciences*, 93(4), 1591-1595, **1996**.
 1577 Shaw, S. M.: Southern Palestine geological map on a Scale 1:250,000 with explanatory notes, *Palestine Geol.*
 1578 *Soc. Publ.*, Jerusalem, **1947**.
 1579 Shenhav, H.: Lower Cretaceous sandstone reservoirs, Israel: petrography, porosity, permeability, *AAPG*
 1580 *Bulletin*, 55(12), 2194-2224, **1971**.
 1581 Sheppard, A. P., Sok, R. M., and Averdunk, H.: Techniques for image enhancement and segmentation of
 1582 tomographic images of porous materials, *Physica A: Statistical mechanics and its applications*, 339(1-2),
 1583 145-151, **2004**.
 1584 Shimron, A. E.: Tectonic evolution of the southern Mount Hermon, *Geological Survey of Israel Report*,
 1585 *GSI/10/98*, **1998**.
 1586 Sneh, A., and Weinberger, R.: Geology of the Metula quadrangle, northern Israel: Implications for the offset
 1587 along the Dead Sea Rift, *Israel Journal of Earth Sciences*, 52, **2003**.
 1588 Sneh, A., and Weinberger, R.: Metula sheet 2-11, *Geology Survey of Israel, Ministry of Energy*, **2014**.
 1589 Tatomir, A. B., Halisch, M., Duschl, F., Peche, A., Wiegand, B., Schaffer, M., Licha, T., Niemi, A., Bensabat,
 1590 J., and Sauter, M.: An integrated core-based analysis for the characterization of flow, transport and
 1591 mineralogical parameters of the Heletz pilot CO₂ storage site reservoir, *International Journal of*
 1592 *Greenhouse Gas Control*, 48, 24-43, **2016**.
 1593 Stephens, D. B., Hsu, K. C., Prieksat, M. A., Ankeny, M. D., Blandford, N., Roth, T. Kelsey, J., Whitworth, J.
 1594 R.: A comparison of estimated and calculated effective porosity. *Hydrogeology Journal*, 6(1), 156-165,
 1595 **1998**.
 1596 Tiab, D., and Donaldson, E. C.: *Petrophysics: Theory and Practice of Measuring Reservoir Rock and Fluid*
 1597 *Transport Properties*, Elsevier, **2004**.
 1598 Tidwell, V. C., and Wilson, J. L.: Permeability upscaling measured on a block of Berea Sandstone: Results
 1599 and interpretation, *Mathematical Geology*, 31(7), 749-769, **1999**.
 1600 Vincent, L., and Soille, P.: Watersheds in digital spaces: an efficient algorithm based on immersion
 1601 simulations, *IEEE Transactions on Pattern Analysis & Machine Intelligence*, 6, 583-598, **1991**.

1602 Vogel, H. J.: Topological characterization of porous media, in: Morphology of condensed matter, edited by:
1603 Mecke, K. R., and Stoyan, D., Springer, Berlin, 75-92, **2002**.

1604 Wang, W. P., Liu, J. L., Zhang, J. B., Li, X. P., Cheng, Y. N., Xin, W. W., & Yan, Y. F. Evaluation of laser
1605 diffraction analysis of particle size distribution of typical soils in China and comparison with the Sieve-
1606 Pipette method. *Soil science*, 178(4), 194-204, **2013**.

1607 Viswanathan, J., Konwar, D., & Jagatheesan, K. Laboratory Characterization of Reservoir Rock and Fluids of
1608 Upper Assam Basin, India. In *Novel Issues on Unsaturated Soil Mechanics and Rock Engineering:
1609 Proceedings of the 2nd GeoMEast International Congress and Exhibition on Sustainable Civil
1610 Infrastructures, Egypt 2018–The Official International Congress of the Soil-Structure Interaction Group
1611 in Egypt (SSIGE)* (p. 179). Springer., **2018**.

1612 Weissbrod, T.: Stratigraphy and correlation of the Lower Cretaceous exposures across the Dead Sea Transform
1613 with emphasis on tracing the Amir Formation in Jordan, *Israel Journal of Earth Sciences*, 51(2), 55–78,
1614 **2002**.

1615 Weissbrod, T., and Nachmias, J.: Stratigraphic significance of heavy minerals in the late Precambrian-
1616 Mesozoic clastic sequence (“Nubian Sandstone”) in the Near East, *Sedimentary Geology*, 47(3-4), 263-
1617 291, **1986**.

1618 Whitaker, S.: Flow in porous media I: A theoretical derivation of Darcy's law, *Transport in porous media*, 1(1),
1619 3-25, **1986**.

1620 Wiegmann, A.: GeoDict, the Digital Material Laboratory - Easy-to-use - Powerful - Accurate, Whitepaper,
1621 **2019**, <https://doi.org/10.30423/WHITEPAPER.M2M-2019>

1622 Wildenschild, D., and Sheppard, A. P.: X-ray imaging and analysis techniques for quantifying pore-scale
1623 structure and processes in subsurface porous medium systems, *Advances in Water Resources*, 51, 217-
1624 246, **2013**.

1625 Zhang, D., Zhang, R., Chen, S., and Soll, W. E.: Pore scale study of flow in porous media: Scale dependency,
1626 REV, and statistical REV, *Geophysical research letters*, 27(8), 1195-1198, **2000**.

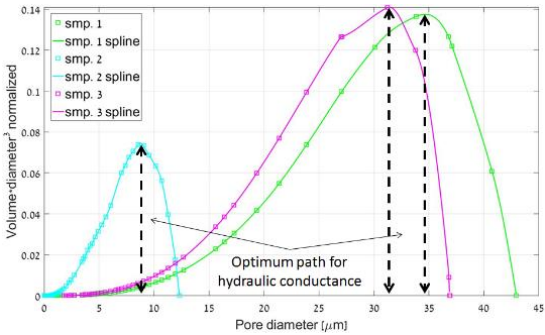
1627 Zhang, P., Leed, Y.I., and Zhange, J.: A review of high-resolution X-ray computed tomography applied to
1628 petroleum geology and a case study, *Micron*, 124, 102702, **2019**.

1629 Zhu, W., Montési, L.G.J., and Wong, T.F.: Effects of Stress on the Anisotropic Development of Permeability
1630 during Mechanical Compaction of Porous Sandstones, *Geological Society, London*, 119-136, Special
1631 Publications, 200, **2002**.

Deleted: Schwanghart, W.: Experimental (Semi-) Variogram (<https://www.mathworks.com/matlabcentral/fileexchange/20355-experimental-semi-variogram>), MATLAB Central File Exchange, **2020a**. ¶
Schwanghart, W . variogramfit (<https://www.mathworks.com/matlabcentral/fileexchange/25948-variogramfit>), MATLAB Central File Exchange, **2020b**. ¶

1644

1645 ~~Appendix A: Maximum hydraulic conductance~~



1646

1647 **Figure A1:** The pore throat length of the maximal hydraulic conductance, l_{max} , is defined from the maximal
1648 (normalized) hydraulic conductance (Katz and Thompson, 1987), specified at the vertical axis of the chart.
1649 The corresponding pore throat diameters (x-axis) marked by black arrows define the pore throat diameters
1650 (or pore throat lengths of maximal conductance), l_{max} , where all connected paths composed of $l \geq l_{max}$
1651 contribute significantly to the hydraulic conductance (see Sect.3.2).

1652

1653

1654

Deleted: Appendix A: Results of the REV determination by the classical approach¶

Deleted: ...

Deleted: Figure A1: Results of the classic REV analysis for sandstones S1-S3 (a,c,e). (b, d, f) Magnified views of the mean and median porosity trends of S1-S3 calculated for varying edge lengths. The scattering of porosity measured for each sub-volume is shown in blue dots. The laboratory porosities measured by gas porosimetry are shown by a pink line. The image porosity for CT, which was predicted by MIP for the resolution limit, is shown by a yellow line. The mean and median porosity are depicted by red and green lines, respectively.¶

Deleted: B

Deleted: B1